

Geoelectric Monitoring of Bentonite Barrier Resaturation in the Äspö Prototype Repository

Final Report



Gesellschaft für Anlagen-
und Reaktorsicherheit
(GRS) gGmbH

Geoelectric Monitoring of Bentonite Barrier Resaturation in the Äspö Prototype Repository

Final Report

Klaus Wieczorek
Michael Komischke
Rüdiger Miehe
Helge Moog

Oktober 2014

Remark:

This report was prepared under contract No. 02E9944 of the German Federal Ministry for Economic Affairs and Energy (BMWi).

The work was conducted by the Gesellschaft für Anlagen- und Reaktorsicherheit (GRS) gGmbH.

The authors are responsible for the content of this report.

GRS - 352
ISBN 978-3-944161-32-7

Keywords

Äspö Hard Rock Laboratory, Bentonite Resaturation, Geoelectric Tomography

Preface

In 1994, SKB started constructing the “Prototype Repository”, a full scale replica of a part of a future KBS-3 repository in crystalline rock, at the Äspö Hard Rock Laboratory. Six emplacement boreholes were planned and constructed in two tunnel sections until end of 1999.

The international EC co-funded Prototype Repository project was started in 2000 (contract FIKW-CT-2000-00055). The project partners were SKB (Sweden), POSIVA (Finland), ENRESA (Spain), GRS (Germany), BGR (Germany), UWC (UK), and JNC (Japan). Between 2000 and 2003 the complete Prototype Repository was equipped and instrumented, and monitoring was started.

In February 2004 the EC funding expired. The Prototype Repository project was continued with national funding of the project partners.

In 2011, dismantling of Section II was started in a three-year project. Backfill, buffer and canisters as well as part of the instrumentation were retrieved, and numerous laboratory investigations on buffer and backfill samples were performed.

GRS' part in the Prototype Repository was the monitoring of backfill and buffer resaturation using geoelectric tomography. The measurements were completed in 2013.

Table of contents

1	Introduction.....	1
2	Objectives	3
3	Fundamentals of geoelectrics	5
3.1	Theory	5
3.2	Measuring technique	8
3.3	Evaluation method.....	9
4	Preparatory work	11
4.1	Laboratory calibration	11
4.1.1	Resistivity of MX-80 bentonite.....	11
4.1.2	Resistivity of the tunnel backfill	17
4.1.3	Resistivity of the rock.....	20
4.1.4	Change of solution composition by interaction with compacted MX-80	21
4.2	Assessment of measurement resolution	33
4.2.1	Backfill	33
4.2.2	Buffer.....	36
5	Instrumentation.....	39
5.1	Measurement system	39
5.2	Electrode arrays and installation procedure	41
5.2.1	Backfill electrodes.....	42
5.2.2	Buffer electrodes.....	46
5.2.3	Rock electrodes.....	49
6	In-situ measurements.....	51
6.1	Backfill Section I	51
6.2	Backfill Section II	55
6.3	Buffer deposition hole #5	57
6.4	Rock Section II	59

7	Injection tests in the laboratory	65
8	Post-test investigations	67
8.1	Electrode inspection	67
8.1.1	Backfill electrodes.....	67
8.1.2	Buffer electrodes.....	68
8.2	Buffer water content.....	70
9	Conclusions	73
	Acknowledgements	75
	References	77
	List of figures.....	81
	List of tables	85

1 Introduction

Within the framework of the Swedish nuclear programme, SKB has constructed a full-scale replica of the deep repository planned for the disposal of spent nuclear fuel in order to simulate part of a future KBS-3 repository to the extent possible. This Prototype Repository was constructed at the Äspö Hard Rock Laboratory at a depth of 450 m below ground. The Prototype Repository includes six deposition holes in which full-size KBS-3 canisters with electrical heaters were placed and surrounded by a bentonite buffer (see Fig. 1.1). The deposition tunnel was backfilled with a mixture of bentonite and crushed granitic rock.

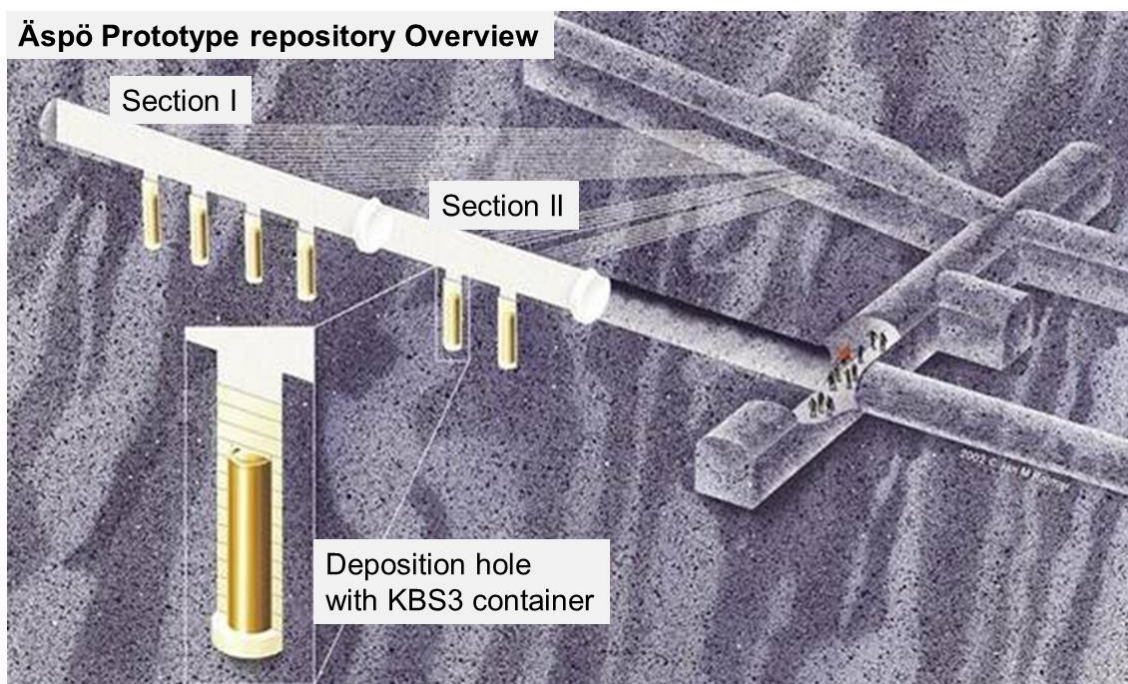


Fig. 1.1 Overview of the Äspö Prototype Repository (modified after /SKB 11/)

The 65 m long test drift was prepared by TBM boring in 1994. The deposition holes of 8 m depth and 1.75 m diameter were bored in 1999 and characterised in terms of straightness, orientation, wall surface topography, petrology, intersection of fractures, and water inflow /SVE 00/. Section I of the Prototype Repository incorporates the four rear deposition holes. It was equipped with canisters and buffer, instrumented and backfilled in 2000/2001 and afterwards sealed with a concrete plug. Subsequently, the two deposition holes of Section II were equipped and instrumented and the tunnel of Section II was backfilled in the same way as Section I.

In this configuration the Prototype Repository was run until the end of 2010. In 2011, excavation of Section II was started. The backfill and the buffer in Section II were completely removed, and the canisters in the deposition holes #5 and #6 were retrieved. A great number of samples were taken and instruments were retrieved for laboratory investigations. In the meantime, Section I has continued to operate.

Water uptake of the bentonite buffer in the deposition holes and of the bentonite/crushed rock backfill in the test tunnel has been one of the central issues to be investigated in the frame of the Prototype Repository Project. GRS has used the geoelectric method to monitor changes in water content, as the electric resistivity of the materials is determined by the solution content. Several electrode arrays in the buffer, the backfill, and the rock served for determining the resistivity distributions in cross sections of the different materials. From the resistivity distribution information on the solution content was derived using the results of calibration measurements on samples at defined conditions.

Two arrays of 36 electrodes were installed in the backfill of Section I and Section II, respectively. Both of them were inclined by 35°, as the electrodes had to be placed on the slope of the backfill material during installation. Measurements in the backfill started in October 2001 (Section I) and June 2003, respectively.

Three electrode chains of 30 electrodes each were installed in vertical boreholes in the rock below the floor of the tunnel of Section II between the deposition holes #5 and #6. Measurements were started in August 2002.

An array of 22 electrodes in the top part of the buffer of deposition hole #5 that also makes use of the adjacent electrodes in the rock started measuring in May 2003.

In the course of the excavation of Section II in 2011, these measurements were stopped, part of the buffer and backfill electrodes were retrieved and inspected, and reasons for electrode failure were determined. Measurements in the backfill of Section I were continued until 2013, when the GRS participation in the Prototype Repository ended.

This report contains a summary of all GRS activities and results in the Prototype Repository Project.

2 Objectives

The main objectives of the Prototype Repository, as given by /SVE 00/, were “to simulate part of a future KBS-3 deep repository to the extent possible with respect to geometry, design, materials, construction and rock environment except that radioactive waste is simulated by electrical heaters, and to test and demonstrate the integrated function of the repository components”. Further objectives concerned development and testing of engineering standards and quality assurance methods as well as confidence building.

GRS’ objectives in the project were to determine the water uptake with time in the backfill and in the buffer and the potential desaturation of the rock around the deposition holes as a consequence of buffer saturation using the geoelectric method, and to show the capability of this method for the investigation of such issues.

3 Fundamentals of geoelectrics

3.1 Theory

In direct current geoelectrics, a stationary electric field is generated in a dielectric by means of two current electrodes. It is measured with two further potential electrodes.

In an isotropic medium, the current density J generated by an electric field E is described by the constitutive equation (Ohm's law),

$$J = \sigma E \quad (3.1)$$

With the exception of laboratory measurements on test samples of known geometry, the electrical conductivity σ is not directly measurable. The value determined by field measurements depends on the geometry of the measuring arrangement and is affected by the inhomogeneity of the structure; it is therefore designated as the apparent electrical conductivity. In practice, the electrical resistivity, that is, the reciprocal of the conductivity, is more frequently employed and is denoted by $\rho = 1/\sigma$.

Since the magnetic field does not vary in the case of a uniform electric current, the magnetic flux density B is constant in time:

$$\partial B / \partial t = 0 \quad (3.2)$$

From Maxwell's equations, it thus follows that $\text{rot } E$ vanishes:

$$\text{rot } E = 0 \quad (3.3)$$

Equation (3.3) indicates that E can be expressed as the gradient of a scalar potential ψ :

$$E = -\text{grad } \psi \quad (3.4)$$

This potential is sufficient because $\text{div } J = \text{div } (\sigma E)$ in the differential equation:

$$\sigma \text{ div grad } \psi = -\text{div } J \quad (3.5)$$

In accordance with Gauss' theorem of vector analysis, the volume integral of the divergence of the current density J over the volume V is equal to the sum of the current sources within the volume V :

$$\int_V \text{div } J dV = I \delta \quad (3.6)$$

δ is the Dirac delta function, which assumes a value of 1 where sources are present and is otherwise equal to zero. For an infinitesimally small volume dV , the following applies:

$$\text{div } J = I \delta \quad (3.7)$$

In accordance with (3.5),

$$\text{div } J = -\sigma \text{div grad } \psi \quad (3.8)$$

applies; hence, Poisson's differential equation is finally obtained for the potential field due to arbitrary current sources:

$$\text{div grad } \psi = -\rho I \delta \quad (3.9)$$

with $\rho = 1/\sigma$.

If it is assumed that the electric field is stationary, E can be derived as an irrotational vector from a potential ψ . If the divergence is determined from (3.4), the following inhomogeneous potential equation is obtained for ψ :

$$\text{div grad } \psi = -\text{div } E \quad (3.10)$$

The right-hand side of this equation is known. With the application of Green's theorem from vector analysis, ψ can be calculated in the following form:

$$4\pi\psi = \int_V \frac{\text{div } E}{r} dV \quad (3.11)$$

With the use of equations (3.11), (3.10), and (3.9), the potential field ψ is thus obtained for a point source:

$$\psi = \frac{1}{4\pi} I\rho \frac{1}{r} \quad (3.12)$$

I is the current which flows through the source, and r is the distance of the point under consideration from the source point for which ψ is being calculated and over whose coordinates the integration is being performed. The source point is also the location of the volume element dV . The potential field of a dipole source results from the superposition of the potential fields for two point sources with positive and negative current:

$$\psi = \psi_1 + \psi_2 = \frac{1}{4\pi} I\rho \left(\frac{1}{r_1} - \frac{1}{r_2} \right) \quad (3.13)$$

r_1 and r_2 denote the distances of the points under consideration from source points 1 and 2, respectively, with the potential fields ψ_1 and ψ_2 . The potential field generated by the dipole source is measured as a potential difference at two potential electrodes. If equation (3.13) is applied at each potential probing point, and if the difference is calculated, the following is obtained:

$$\Delta\psi = \frac{1}{4\pi} I\rho \left(\frac{1}{r_{11}} - \frac{1}{r_{12}} - \frac{1}{r_{21}} + \frac{1}{r_{22}} \right) \quad (3.14)$$

r_{ij} is the distance of the i^{th} potential electrode from the j^{th} current electrode. The expression between brackets is denoted by $1/K$ for brevity. K is designated as a geometric factor.

During a measurement, the potential difference as well as the supplied current are measured, and the resistance is determined. This value is the sum of the resistances between the current electrodes and the contact resistances at the electrodes; it is an apparent resistance. The true resistivity is equal to the apparent resistivity only in a homogeneous medium. The apparent resistivity is given by:

$$\rho = 4\pi \frac{\Delta\psi}{I} K \quad (3.15)$$

In geoelectrics, a wide variety of electrode arrangements are employed.

As a rule, geoelectrics is applied on profiles at the earth's surface, where the factor 4π (three-dimensional space) in (3.15) is replaced by the factor 2π (half space); that is, the problem under investigation is two-dimensional. In three-dimensional space, the electrodes are spatially distributed, either in an array on the surface or in boreholes.

3.2 Measuring technique

The technique most frequently applied for geoelectric measurements in the field is the four-point method (Fig. 2.1). An electric current is supplied to the formation at two electrodes. The magnitude and direction of the resulting electric field are dependent on the conductivity distribution in the rock. The measurements are performed by means of a further pair of electrodes; for this purpose, the difference between the potentials at the electrodes is determined. The input electrodes (C1, C2) and the output electrodes (P1, P2) are arranged as single dipoles (Fig. 3.1). For a complete data set, the position of the input dipole is fixed and the output dipole is moved around the area to be investigated. Afterwards, the input dipole is moved to another position, and the measurements are repeated. From the measured potential difference (voltage) and the supplied current, the value of the electrical resistivity is obtained in accordance with Ohm's law, with due consideration of the relative position of the four electrodes with respect to one another. In the normal case of a spatial varying resistivity, a large number of single measurements with different injection and measurement dipoles is needed.

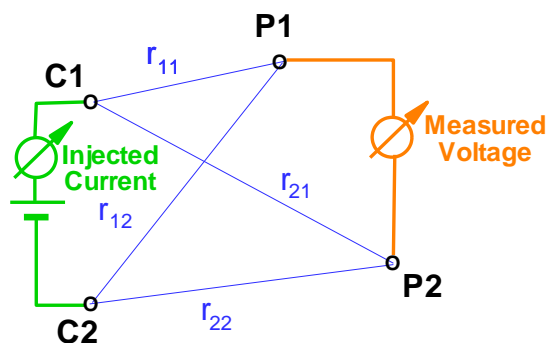


Fig. 3.1 Principle configuration of a dipole-dipole measurement

Although methods of direct current geoelectrics are employed for the evaluation of geoelectric measurements, modern resistivity meters use low-frequency alternating current rather than direct current. The reasons are:

- Direct current would cause electrolytic polarization, i. e. build-up of ions around the electrodes. This is prevented by periodic reversal of the current.
- Telluric currents, i. e. natural electric currents in the ground, can be accounted for in the measurements when the current is reversed and the measurement results are averaged, since the telluric currents do not change their polarity.

3.3 Evaluation method

Measurement evaluation is performed by inverse finite element modelling. Starting with a usually homogeneous model, the expected vector of apparent resistivities for the set of measurement configurations is calculated and compared to the actually measured apparent resistivities. The model is then iteratively improved in order to minimize the deviations between calculated and measured values.

The finite element mesh has to be adapted to the electrode array. The maximum attainable resolution is half the electrode spacing; this is the minimum side length of the finite elements. On the other hand, the attainable resolution has to be considered when designing the electrode array. Half the electrode spacing is the theoretically maximum attainable resolution – if an electrode was placed at every second grid point of the mesh, the inversion result would be definite. In reality, such a high number of electrodes and related measurement configurations are not feasible. Consequently, there are areas further away from electrodes where resolution and accuracy decrease. Therefore, scoping calculations were performed in order to optimize the layout of the electrode array and assess the measurement resolution (see Section 4.2).

For the evaluation of the measurements, GRS uses the commercial software package SensInv2D /FEC 01/ which allows a two-dimensional inversion of the measured apparent resistivity data. Several strategies for applying iterative improvements to the resistivity model are implemented in this software. GRS employs the multiplicative simultaneous inversion reconstruction technique (MSIRT) /KEM 95/ which is controlled by the cumulative sensitivity distribution of the model. Each single measurement configuration gives a so-called sensitivity distribution, which is the matrix of partial

derivatives of measured impedance against resistivity. Thus, the sensitivity at a special finite element describes how sensitive the measurement result is to changes in resistivity. The cumulative sensitivity is the sum of the sensitivity matrices of all single measurements, thus describing where a resistivity change has a high influence on the overall results, and where not. Cumulative sensitivity is usually highest near the electrodes and lowest farther away.

Evaluation of the geoelectric measurements leads to a two-dimensional resistivity distribution that is supposed to be close to the true resistivity field. The resistivity distribution is made visible as a contour plot, a tomographic image. In order to interpret this resistivity distribution in terms of water content distribution, laboratory measurements were performed using samples of defined water content (see Section 4.1). Using the results of the laboratory calibrations, information on water content can be derived from the resistivity distribution.

4 Preparatory work

4.1 Laboratory calibration

In order to enable interpretation of the in-situ resistivity measurements in terms of water content, calibration measurements on the materials present in the Prototype Repository were performed at GRS' geotechnical laboratory in Braunschweig.

The calibrations include the determination of the resistivity of compacted MX-80 powder and of original pre-compacted buffer material samples provided by SKB as well as of the drift backfill, all materials in dependence of their water content and of temperature. For the crystalline host rock, data from earlier projects were available.

Besides its dependence on the water content, the electric resistivity is also a function of salinity and composition of the pore solution. Since both may change as the solution penetrates the buffer and the backfill, investigations were performed in order to quantify this effect.

4.1.1 Resistivity of MX-80 bentonite

4.1.1.1 Preparation of compacted MX-80 samples with defined water content

For the preparation of MX-80 samples with different water contents, the MX-80 powder was moisturized with ÄSPÖ-solution with the composition shown in Tab. 4.1. By drying the MX-80 powder in an oven at 105 °C for 24 h, the water content of the delivered MX-80 material was determined to 9.8 wt%. Under consideration of this value, the total water content of the samples was obtained by adding an adequate amount of Äspö solution.

Subsequently, the moist powder was compacted in a specially constructed resistivity measurement cell (see Fig. 4.1) to a dry density of 1.66 g/cm³ which is considered a representative value for the conditions at the top of a deposition borehole /DAH 98/. For each water content value a new sample was produced. The specifications of prepared samples and their water content are shown in Tab. 4.2.

Tab. 4.1 Composition of the ÄSPÖ solution [mmol/l] used for sample preparation

Na	K	Ca	Mg	Cl	SO ₄
79.67	0.25	17.06	3.33	113.92	3.40

Tab. 4.2 Water content and size of the prepared MX-80 samples and of the original buffer samples

Sample	Water content wt %	Sample length mm	Sample diameter mm
Compacted MX-80 samples			
MX-80/1	11	100.0	40
MX-80/2	16	100.0	40
MX-80/3	22	96.1	40
MX-80/3a	22	95.0	40
MX-80/4	27	86.4	40
MX-80/5	33	87.1	40
Samples from original ÄSPÖ buffer material			
ÄSPÖ-PR-BFST 13/1	13	97	50
ÄSPÖ-PR-BFST 13/2	12	97	50
ÄSPÖ-PR-BFST 13/3	12	97	50
ÄSPÖ-PR-BFST 17/1	14	97	50
ÄSPÖ-PR-BFST 17/2	14	97	50
ÄSPÖ-PR-BFST 17/3	14	91	50

4.1.1.2 Preparation of original ÄSPÖ MX-80 buffer samples

Cylindrical samples were prepared from original bentonite bricks provided by SKB. These samples had different initial water contents of about 13 and 17 wt%, respectively. Three samples were prepared from the 13-wt% material and marked ÄSPÖ-PR-BFST 13/1 to 13/3 and three further samples from the 17-wt% material marked ÄSPÖ-PR-BFST 17/1 to 17/3. The water content of the original bricks was determined on material remaining from sample preparation by drying in an oven at 105 °C for 24 h. The size of the samples and their water content at time of investigation are summarized in Tab. 4.2.

4.1.1.3 Measurement and evaluation

The resistivities of the compacted MX-80 samples with varying water content were measured at ambient temperature in the specially constructed cell shown in Fig. 4.2. At both ends of a Plexiglass tube the current electrodes A and B were installed. Since the samples varied in length, the electrode B was moveable. Two brass rings (voltage electrodes M and N) were inserted in the Plexiglass tube.

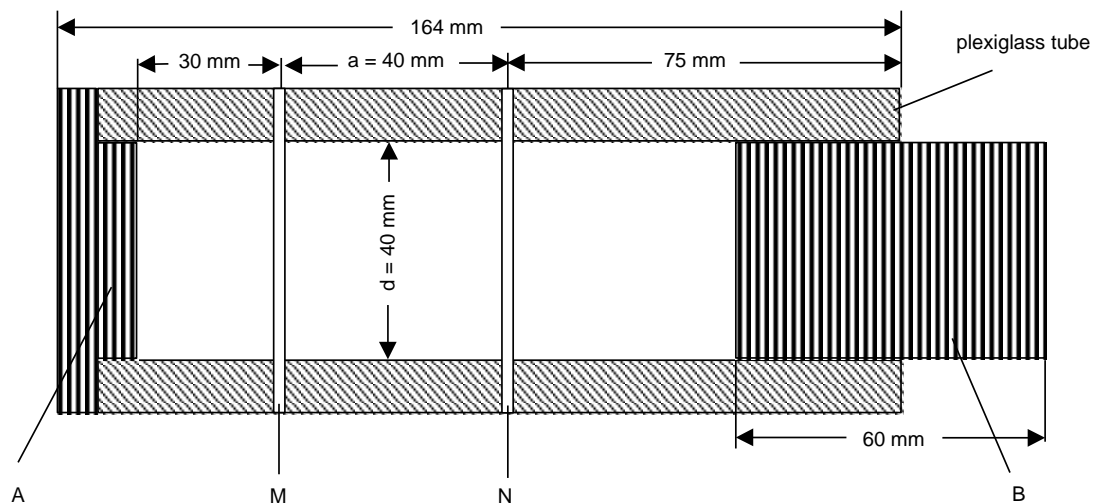


Fig. 4.1 Schematic view of the resistivity measurement cell for compacted MX-80 samples

For the resistivity measurement of the samples prepared from the original bricks, the cylindrical samples were set between two metal plates A and B (Fig. 3.2). A potential difference U was measured at the electrodes M and N which were installed at the surface of the sample.

The resistivity of the samples was determined using the four-point method. The current I was injected at the current electrodes A and B on both sides of the sample and the difference in the electrical potentials U was measured at the voltage electrodes M and N. Following /Sch 73/, the resistivity was calculated by:

$$\rho = \frac{U \cdot A}{I \cdot a} \quad (4.1)$$

with:

ρ = resistivity [Ωm]

U = electrical voltage [V]

I = current [A]

a = distance of the voltage electrodes M and N

A = surface area of the sample [m^2]

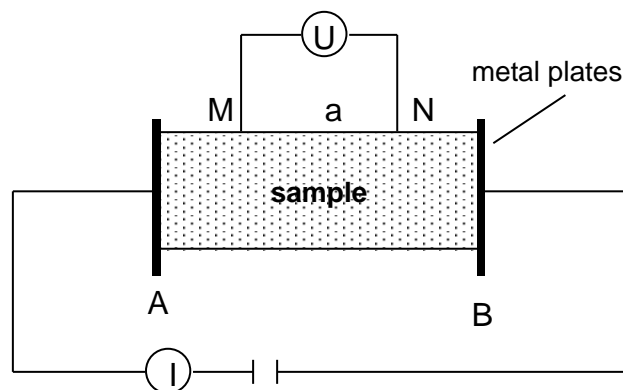


Fig. 4.2 Schematic experiment layout for the determination of sample resistivity

4.1.1.4 Results

The results show that the resistivity of the compacted MX-80 samples decreases with increasing water content (Fig. 4.3). The resistivity ranges between 34.5 and 1.6 Ωm . The water content varies between 11 and 33 wt%. The highest resistivity (34.5 Ωm) was measured at the lowest water content of 11 wt%. A small increase of the water content to 16 wt% already leads to a significant decrease of resistivity (6.8 Ωm). At

higher water contents above 22 wt% up to 33 wt%, the change of resistivity is small (below 2 Ωm).

The resistivity of the original buffer material ranges between 6.3 Ωm and 7.8 Ωm at water contents of about 12 and 13 wt% (samples ÄSPÖ-PR-BFST 13/1 to 13/3) and 3.8 Ωm and 4.5 Ωm at water contents of about 14 wt% (samples ÄSPÖ-PR-BFST 17/1 to 17/3). The resistivity values are in the same range as those of the compacted MX-80 samples at comparable water contents. The water content and the corresponding resistivity values are summarized in Tab. 4.3.

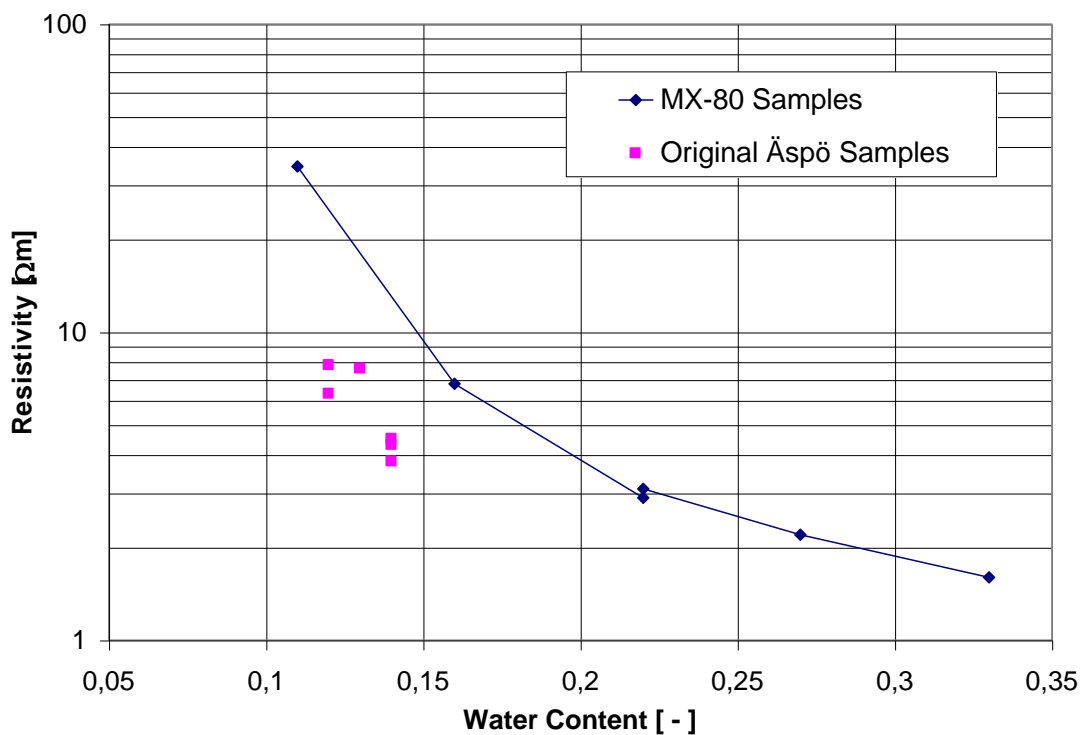


Fig. 4.3 Resistivity of compacted MX-80 samples and original ÄSPÖ buffer material as a function of the water content

The steep drop of resistivity at the lower water contents can be explained by a clay-typical interface conductivity which is due to additional cations held loosely in the diffuse part of the electrical double layer surrounding the clay particles /SER 84/. Already a small amount of solution leads to formation of a double layer and causes the interface conductivity.

Tab. 4.3 Summary of the water content and the resistivities of the compacted MX-80 samples and the original ÄSPÖ buffer material

MX-80 sample	water content wt%	Resistivity Ωm
compacted MX-80 samples		
MX-80/1	11	34.5
MX-80/2	16	6.8
MX-80/3	22	2.9
MX-80/3a	22	3.1
MX-80/4	27	2.2
MX-80/5	33	1.6
samples from original ÄSPÖ buffer material		
ÄSPÖ-PR-BFST 13/1	13	7.6
ÄSPÖ-PR-BFST 13/2	12	6.3
ÄSPÖ-PR-BFST 13/3	12	7.8
ÄSPÖ-PR-BFST 17/1	14	3.8
ÄSPÖ-PR-BFST 17/2	14	4.5
ÄSPÖ-PR-BFST 17/3	14	4.3

Because of the relatively small resistivity changes observed at higher saturation it seems obvious that the interface conductivity is the predominant part of the conductivity in the MX-80 bentonite.

The total conductivity is a sum of the conductivity of the free solution in the pore space and the interface conductivity. According to /SCH 82/, the conductivity of a solution saturated porous rock can be described by

$$\sigma_0 = \frac{1}{F} \sigma_w + \sigma_{q0} \quad (4.2)$$

with the total conductivity of the fully saturated rock σ_0 , the formation factor F , the electrolytic solution conductivity σ_w , and the interface conductivity σ_{q0} .

4.1.2 Resistivity of the tunnel backfill

4.1.2.1 Samples

The backfill samples were prepared with properties representative for the conditions right after installation. This means a design density of 1.7 g/cm^3 and an initial water content of 12 wt%, implying a dry density of the backfill of 1.5 g/cm^3 .

The initial water content of both the crushed rock and the Milos bentonite were determined according to DIN 18121-1 /DIN 89/ by drying in an oven for 90 hours at $105 \text{ }^\circ\text{C}$ and subsequent measurement of the weight loss. According to the measurements, the crushed rock had an initial water content of 1.20 wt% and the Milos bentonite of 13.09 wt%.

Samples of backfill with different water content were prepared by first mixing pure crushed rock and Milos bentonite as delivered by SKB and subsequent spraying of predetermined amounts of Äspö water (compare Tab. 3.1) into the material until the desired total water content was achieved. Seven samples were prepared, their properties are summarized in Tab. 4.4.

Figure 4.4 shows emplacement of the moisturized material into the specially designed and fabricated measurement cell, and Fig. 4.5 shows a four-point-measurement set-up. All samples were manually compacted as far as possible to achieve the dry density of 1.5 g/cm^3 . Especially at the highest water content of 33 wt% it was impossible to achieve the dry density of 1.5 g/cm^3 because the material was very sticky. For the determination of electrical conductivity or resistivity, however, all samples were considered acceptable.

Tab. 4.4 Water content and achieved dry density of backfill samples

Backfill sample	Water content wt%	Achieved dry density g/cm³
Sample 1	12	1.33
Sample 2	13	1.53
Sample 3	15	1.45
Sample 4	18	1.48
Sample 5	21	1.50
Sample 6	25	1.51
Sample 7	33	1.27



Fig. 4.4 Emplacement of moisturized backfill into measurement cell for determination of material resistivity



Fig. 4.5 Measurement set-up for determination of backfill resistivity

4.1.2.2 Results

For different water contents, the resistivity measurements of the compacted crushed rock/Milos bentonite samples were performed at 22 °C and 35 °C. The results are presented in Fig. 4.6. Both resistivity curves show a decrease in resistivity with increasing water content. The resistivity measured at 22 °C ranges between 16.3 Ωm and 1.9 Ωm at water contents between 12 wt% and 33 wt%. The resistivity values measured at 35 °C are lower and range between 9.7 Ωm and 1.7 Ωm at comparable water contents. These results are in good agreement with the results obtained on compacted MX-80 samples and original ÄSPÖ MX-80 buffer samples and show the same characteristic steep resistivity decrease at lower water contents. Because of the similar behaviour of buffer and backfill it is concluded in addition that the bentonite governs the resistivity behaviour of the backfill.

The resistivity values at the higher temperature (35 °C) are lower than the values measured at 22 °C. This is explained by the temperature dependence of the pore solution, because the conductivity of most electrolyte solutions increases with increasing temperature. But it can be caused by the temperature influence on the resistivity of the bentonite or the rock material, too. For a better interpretation, appropriate investigations would be necessary.

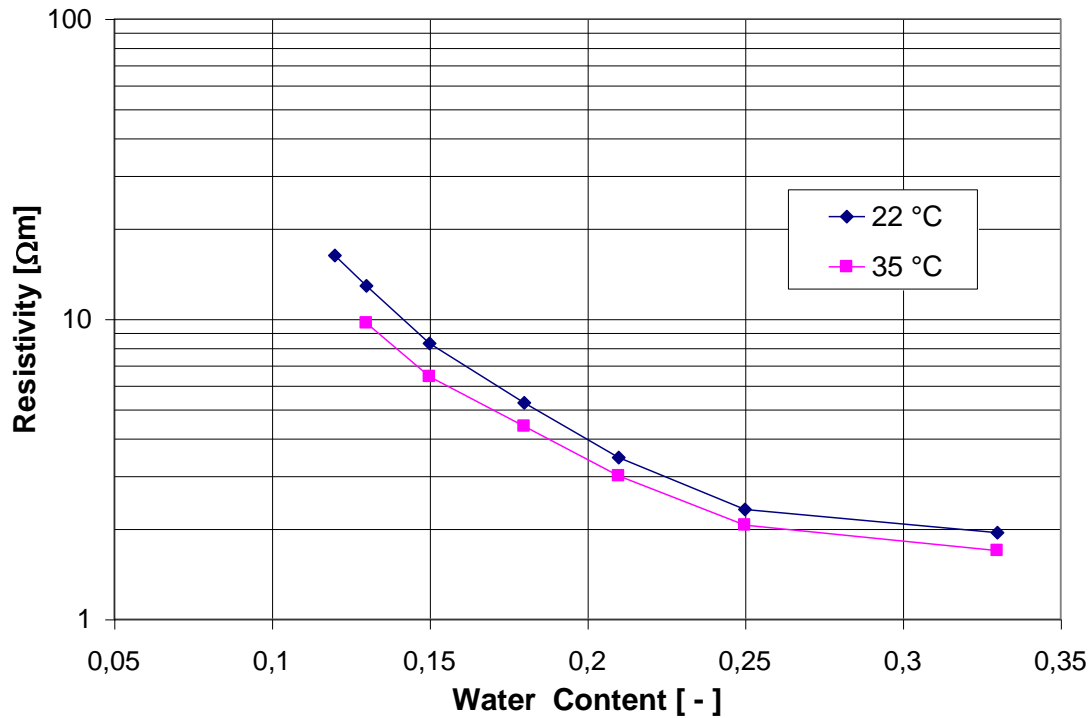


Fig. 4.6 Resistivity of compacted backfill samples versus water content

4.1.3 Resistivity of the rock

Regarding the crystalline rock, calibration results are available from earlier laboratory measurements /ZIM 01/. Six samples of Äspö granite from the ZEDEX drift were saturated with original formation water. For a full saturation of the granite which implies a water content of approximately 0.5 vol%, a resistivity of 1000 Ωm was measured. Afterwards, the samples were dried to decrease the water content. Due to the lower water content, the resistivity increased. The results are shown in Fig. 4.7.

The electric resistivity of the samples was measured as shown in Fig. 4.2 by applying a known voltage to the end planes of the sample and measuring the resulting current. To achieve a good coupling between the metal plates and the sample, the end planes of three of the samples were coated by highly conductive silver paint. The three samples which were measured with silver-coated planes show less scattering of the values compared to the samples without a silver-coating.

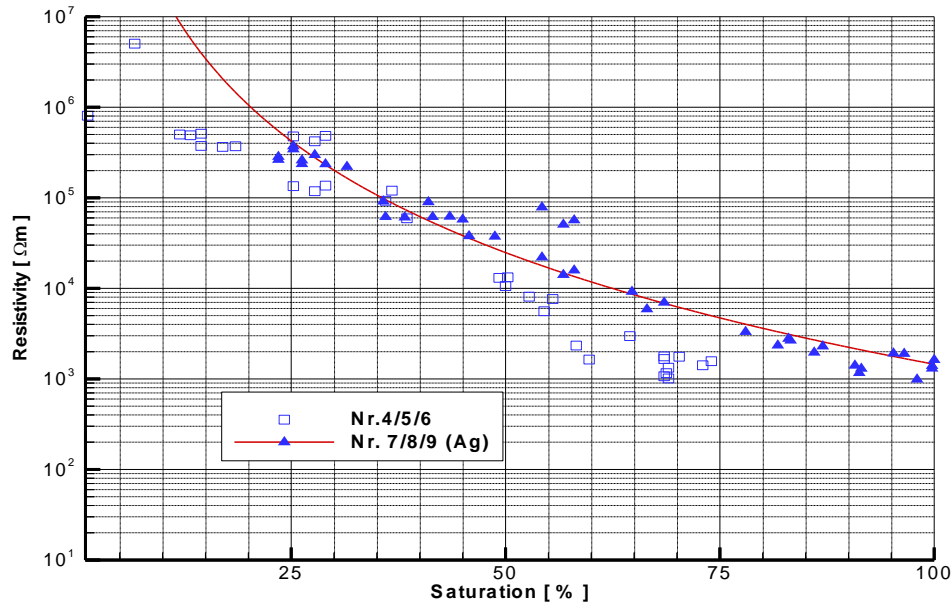


Fig. 4.7 Correlation between resistivity and saturation on granite samples from HRL Äspö

In case of rocks with constant porosity, the relation between resistivity and water content is described by Archie's law, equation (4.3). In this equation, ρ is the total resistivity of the rock, ρ_w the resistivity of the water, Φ the porosity, S the saturation, m the so-called cementation factor, and n the saturation exponent. With this law, the determined values can be fitted by an exponential curve and the constants in Archie's law can be specified.

$$\rho = \rho_w \cdot (\Phi \cdot S)^{-m} \tag{4.3a}$$

$$\rho = \rho_w \cdot \Phi^{-m} \cdot S^{-n} \tag{4.3b}$$

4.1.4 Change of solution composition by interaction with compacted MX-80

These experimental investigations intend to give information about the change of composition which Äspö solution might experience on its way through compacted MX-80. For the situation given in a deposition borehole filled with blocks of compacted bentonite it seemed possible that infiltrating solution changes composition not only due to cation exchange processes. It is the micro structure of the built-in material which induces additional effects. Ultrafiltration of solution (the separation of dissolved salts and water) must not be excluded a priori. The phenomenon of ultrafiltration with

compacted clays has been described and investigated extensively elsewhere, e. g., /HAN 73/, /KHA 73/, /KHA 76/, /DEM 88a/, /DEM 88b/, /DRE 63/, /KEM 64/, /MAR 48/, /KEM 63/, /BEN 84/, /ISH 96/. Within the context of this report it is important to note that compaction density, sample height, particle size (or even size of pellets), and method of compaction may have an impact on the course of percolate composition during an experiment. Further, the rate of flow has an impact on the efficiency of ultrafiltration.

For the reasons given, data gained by batch experiments with suspended clay don't give reliable information on the change of solution during infiltration. As the electrical conductivity of aqueous solution depends on mass and composition of its solutes, the change in electrical conductivity for the system compacted bentonite-salt-water may change while the actual water content remains the same. To quantify the possible impact of change in solution composition on the electrical conductivity of partially saturated bentonite it is necessary to know the change of solute composition as Äspö solution protrudes into the clay barrier.

4.1.4.1 Materials and methods

The experiment being conducted is done with a cell normally taken for the determination of swelling pressures. The bottom frit of the pressure cell was covered with filter paper to prevent it from clogging. 16.1 g of MX-80 representatively probed were placed on it and treated with a spatula to produce an approximately horizontal surface. Compaction proceeded with ca. 1 MPa/min (with sample radius of 2.5 cm, this gives 1901 N/min) to a sample height of 0.51 cm giving a dry density of 1.66 g/cm³.

Compaction pressure was held constant for 15 min to ensure de-aeration of the sample. Then the sample was allowed to relax by unloading it. After 1 min, the sample was compacted again to the desired height and the load held constant for again 15 min. This procedure was repeated until no relaxation occurred anymore and thereby a sample was obtained consolidated at a dry density of 1.66 g/cm³. The uncertainty of dry density was ± 0.01 g/cm³.

The piston was fixed with the screw cap on top. This way, the exact geometry of the sample is known throughout the experiment. The general set up of the experiment is shown in Fig. 4.8. Planning data for the experiment are compiled in Tab. 4.5.

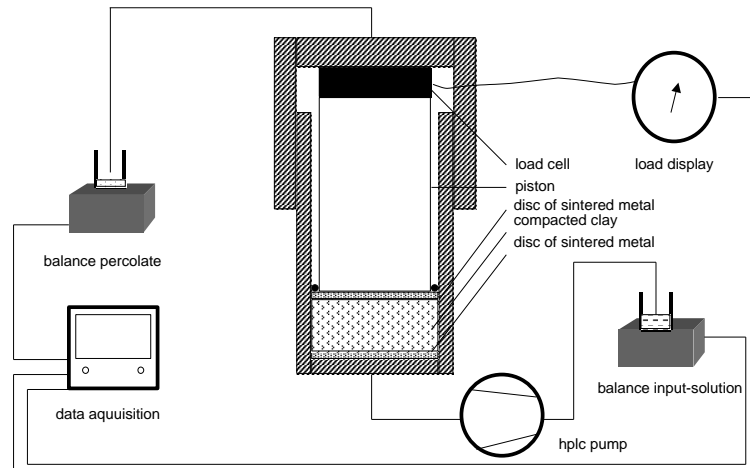


Fig. 4.8 Experimental set-up of percolation experiment

The gas-filled headspaces of the containments for both inflowing and outflowing solution were connected via capillary tubes with small bottles of Äspö solution to prevent evaporation during the experiment. Containments for outflowing solution were changed at intervals ranging between 1 and 4 days. By appropriate weighing an exact mass balance was maintained for inflowing and outflowing solution, and hence for the percolated bentonite.

The HPLC pump delivers the solution at a constant rate of 0.0020 ± 0.0003 ml/min up to a maximum fluid pressure of 47 bar. This corresponds to the maximum likely hydrostatic pressure in the Äspö URL. Also the pump rate compares well with the maximum seepage rate given by SKB. The experiment is run under ambient temperature conditions, which by daily measurement is given with 22.1 ± 0.7 °C.

The discontinuously taken percolates are characterized by the measurement of their density and concentrations of Na, K, Mg, Ca, and SO₄. Concentration of chloride is calculated by difference.

The composition of inflowing "Äspö solution" was calculated as the mean of 55 single sets of analytical data as delivered by SKB. Minor solute components were neglected. With a small correction for electro-neutrality, the composition given in Tab. 4.1 was obtained. Figure 4.9 gives an overview of the variation of probed Äspö solution with sampling date.

Tab. 4.5 Planning data for percolation experiment

Quantity	Symbol	Value	Unit
Diameter of sample	$r =$	2.46	[cm]
Height of sample	$h =$	0.51	[cm]
Volume of sample	$V =$	9.7	[cm ³]
Grain density of MX-80	$\rho_G =$	2.439	[g/cm ³]
Target density	$\rho_{\text{Target}} =$	1.66	[g/cm ³]
Necessary mass of MX-80	$m_{\text{Clay}} =$	16.1	[g]
CEC	$\text{CEC} =$	0.73	[mol _c /kg]
CEC of sample	$\text{CEC}_{\text{Sample}} =$	0.01175	[mol _c]
Grain volume of sample	$V_G =$	6.6	[cm ³]
Remaining pore volume	$V_P =$	3.1	[cm ³]
Normality of Äspö solution	$N_{\text{Solution}} =$	120.58	[mmol/l]
Charges in 1 pore volume Äspö solution	$q_{VP} =$	0.00037	[mol _c]
Necessary pore volumes for 1 x CEC _{Sample}	$n_{VP} =$	31.5	[-]
... corresponding to	$V_{\text{CEC}} =$	97.4	[cm ³]
Powder density of MX-80	$\rho_{\text{bed}} =$	1.034	[g/cm ³]
Bed depth	$h_{\text{bed}} =$	0.82	[cm]
Target rate of flow	$J_{\text{normed}} =$	1	[cm ³ /cm ² *d]
Cross sectional area of sample	$A =$	19.0	[cm ²]
Total rate of flow	$J =$	19.0	[cm ³ /d]
... corresponding to	$J =$	0.79	[cm ³ /h]
... corresponding to	$J =$	0.013	[cm ³ /min]

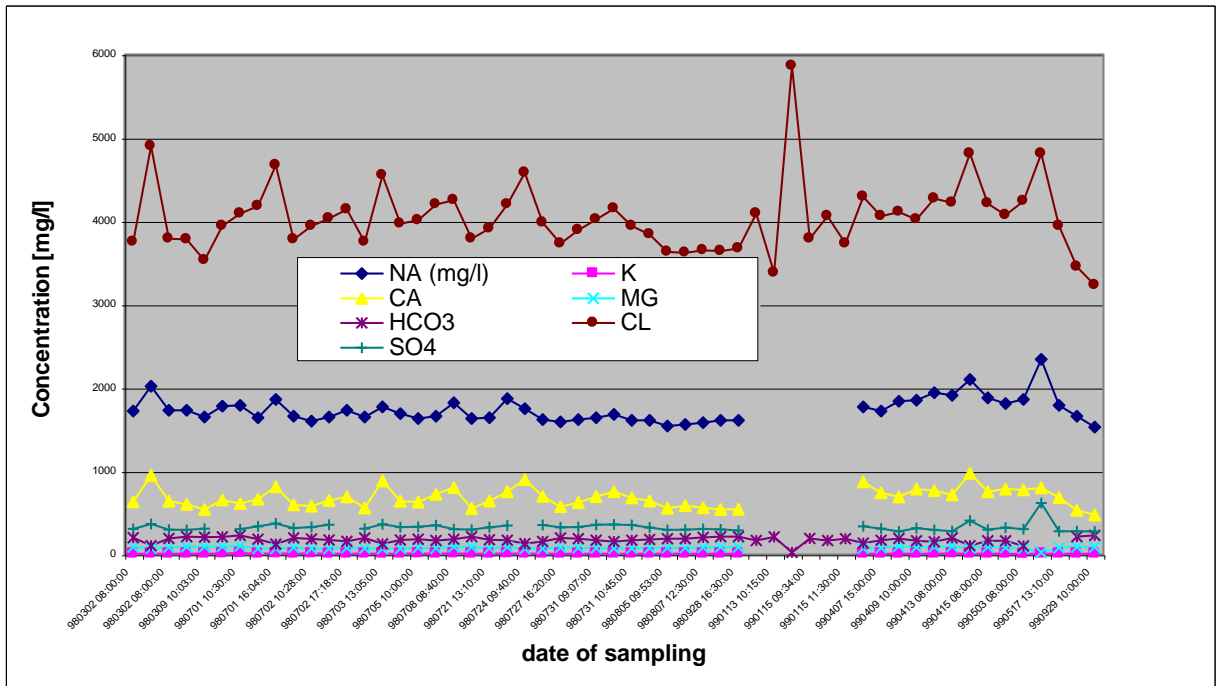


Fig. 4.9 Composition of Äspö solution. All concentrations in mg/l

4.1.4.2 Results

The change in solution composition is depicted in Fig. 4.11 to Fig. 4.16. All measured concentrations were related to the total mass of percolated solution. This is not exactly, but nearly the mass of water percolated. The first data point in all cases represents the inflowing Äspö solution. Its value is marked by a horizontal "baseline" in each figure. In general, it may be concluded that at the beginning of the experiment the sample takes up Mg and Ca from solution while Na and K are being released. The second data point (which represents the first solution having left the sample) indicates dissolution of some minor components of MX-80. As the normality of percolate remains to be higher than that of Äspö-solution, this process seemingly remains to continue during the whole experiment. It cannot be explained with cation exchange. This becomes obvious when the normality of the percolate is regarded (Fig. 4.10). It is defined as

$$N = c_{Na} + c_K + 2 \cdot (c_{Mg} + c_{Ca}) \quad (4.4)$$

With the first solution entering the clay, salt is mobilized which adds to the total salinity introduced by the Äspö solution. On the grounds of purely cation exchange reasoning, also the increase in sulfate would not be expected. This might be due to the oxidation

of pyrite present in the material. The content of chloride was calculated from the charge difference of the cations (Na, K, Mg, Ca) and sulfate.

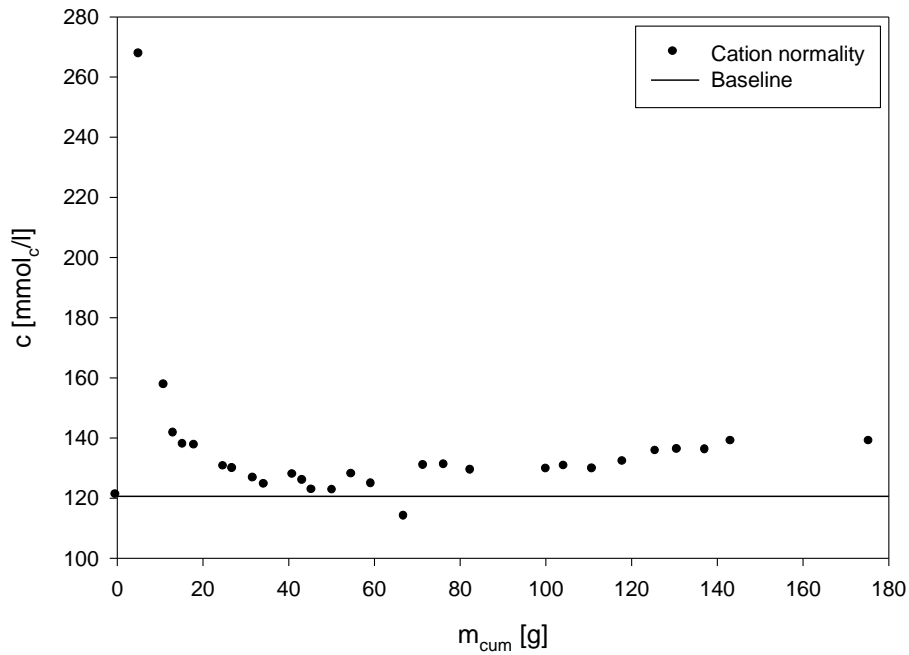


Fig. 4.10 Change of normality of percolate. Note that normality is constantly a bit higher than that of inflowing solution

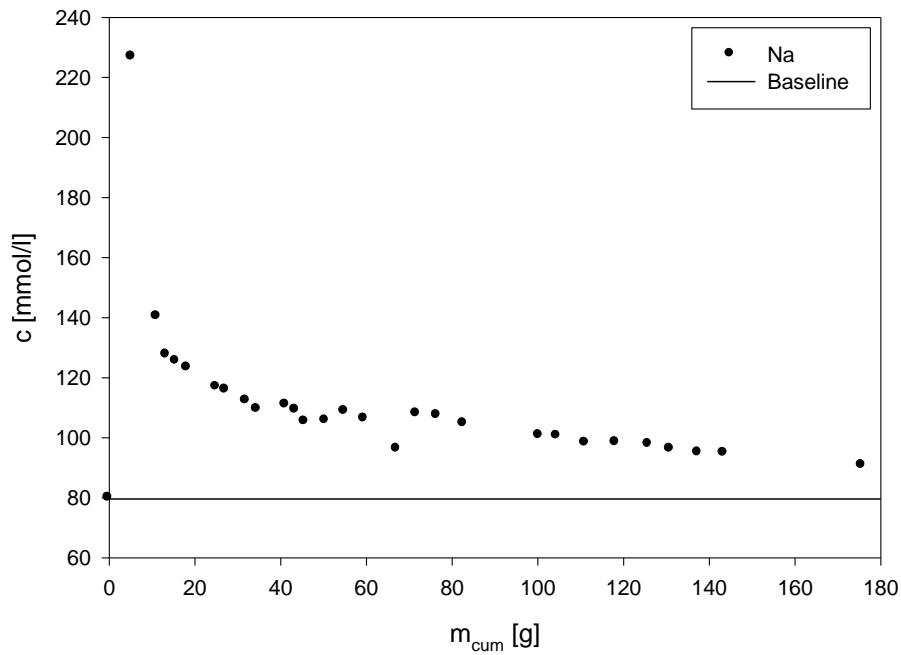


Fig. 4.11 Na-concentration in Äspö-solution after penetrating compacted MX-80

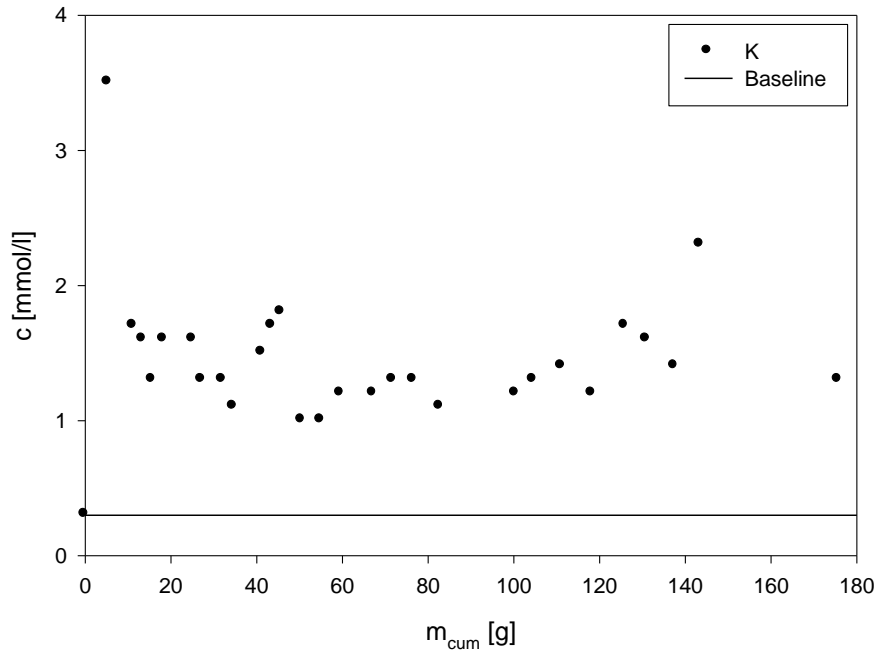


Fig. 4.12 K-concentration in Äspö-solution after penetrating compacted MX-80

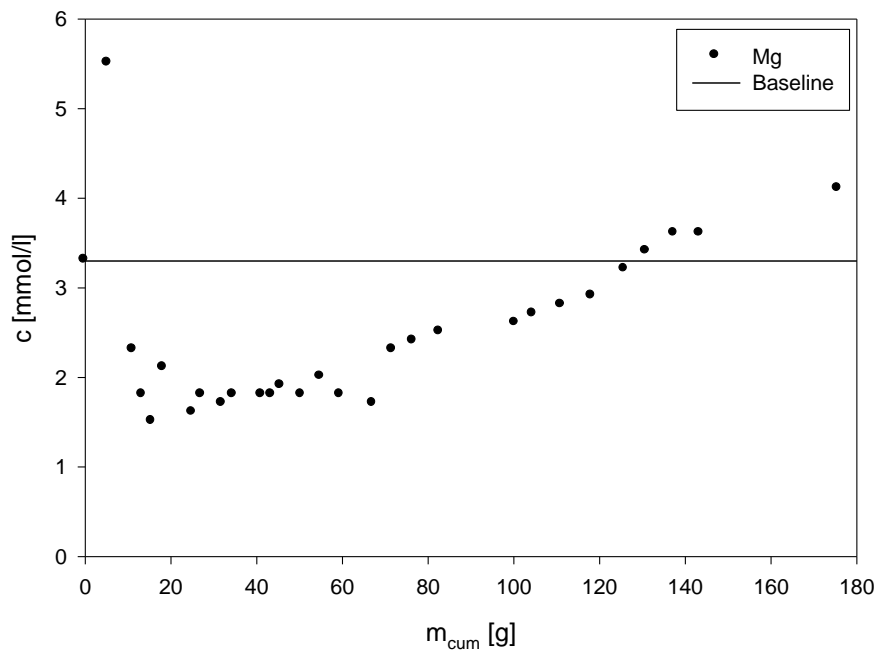


Fig. 4.13 Mg-concentration in Äspö-solution after penetrating compacted MX-80

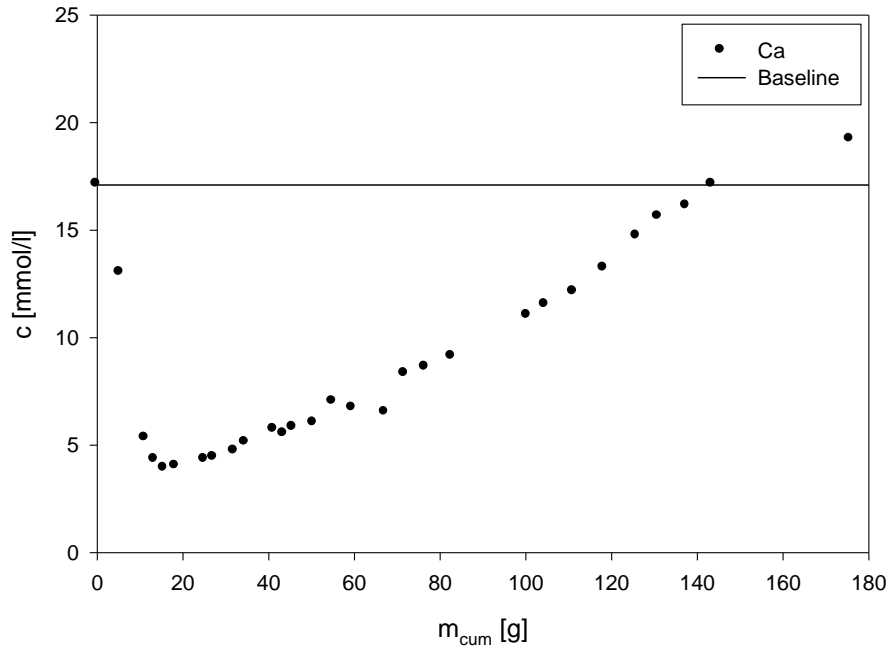


Fig. 4.14 Ca-concentration in Äspö-solution after penetrating compacted MX-80

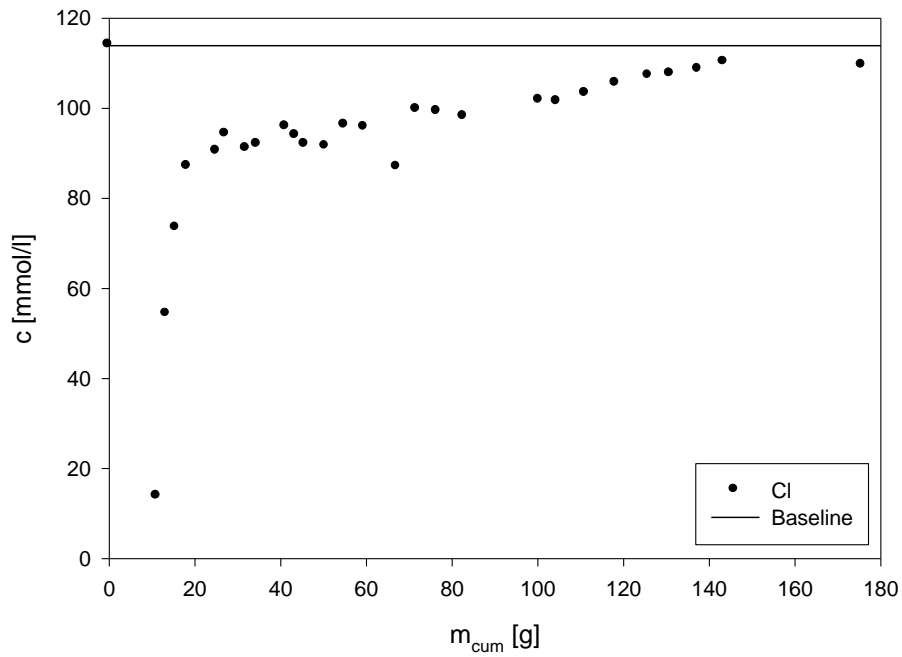


Fig. 4.15 Cl-concentration in Äspö-solution after penetrating compacted MX-80

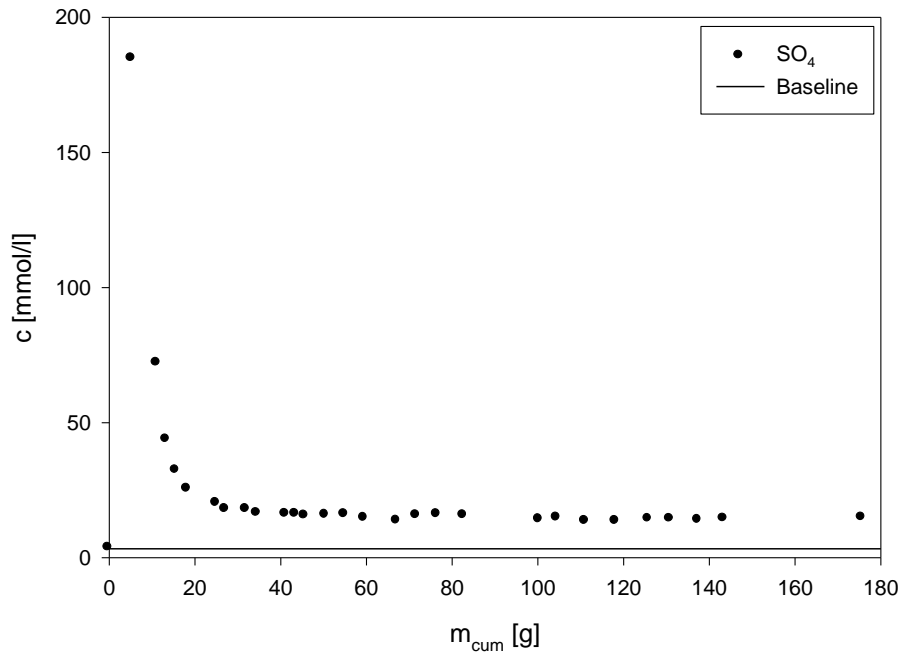


Fig. 4.16 SO_4 -concentration in Äspö-solution after penetrating compacted MX-80

Figure 4.15 shows that the content of chloride in the very first volume increments is replaced in favour of sulfate. At the present state of the experiment, chloride concentration is still lower than that of the inflowing solution, while in the contrary, sulphate continues to be mobilized from the sample.

From the salt content in the percolate, the compacted MX-80 under the given conditions of salinity, flow rate, and compaction density does not seem to behave like a semipermeable membrane. After an initial increase in salinity, the overall salt content in terms of normality comes very close to but is not exactly like the one of the inflowing solution.

Generally, three processes can possibly occur within the sample: cation exchange, mineral dissolution, and ultrafiltration.

Cation exchange. At low ionic strengths this reaction proceeds charge-neutrally. That means that for any charge transferred into the adsorber phase a same charge is *exchanged* into the solution phase. Due to the formation of chloro complexes with alkaline earth metals, this law seemingly is not fulfilled. What is the extent of chloro complex building in Äspö-solution? Taken the stability constant for CaCl^+ at 298.15 K and 1 atm pressure /JOH 79/, /JOH 81/:

$$\log K_{\text{CaCl}^+} = 0,42 \quad (4.5)$$

This is in a certain proportion to the conditional stability constant /SPO 89/:

$$\log K_{\text{CaCl}^+} = \log^c K_{\text{CaCl}^+} + 0,512 \left[\frac{\sqrt{I}}{1 + \sqrt{I}} - 0,3I \right] \Delta Z^2 \quad (4.6)$$

with

$$\Delta Z^2 \equiv \nu_c m^2 + \gamma + \nu_a I^2 - (\nu_c m + \gamma - \nu_a I)^2 \quad (4.7)$$

In the preceding equation, the valences of any constituent building up the complex with the general formula $M_{\nu_c}^{m+} H_{\nu_h}^+ L_{\nu_a}^{l-}$ are accounted for. With the ionic strength pertinent for Äspö-solution, equations (4.5) and (4.6) give after rearrangement:

$$\frac{[\text{CaCl}^+]}{[\text{Ca}^{2+}]} = 10^{0,18} [\text{Cl}^-] \quad (4.8)$$

Equation (4.8) may be solved iteratively to give a set of mutually consistent sets of constituent-concentrations, $\log_c K_{\text{CaCl}^+}$ and ionic strength. For the present purpose it might be sufficient to make an *estimate* by introducing the pertinent chloride concentration in Äspö-solution. The result is that about 17% of calcium (and presumeably Mg) is present as monovalent chloro complex, giving rise to (seemingly) non-electroneutral cation exchange. Practically, this means for the present case that by the adsorption of Ca and Mg (as CaCl^+ and MgCl^+ , respectively) cation normality in solution *decreases*.

The observed change of composition of percolate indicates that Mg and Ca are adsorbed in favour of Na and K. It is hypothesized that both cations are at least partially adsorbed in the form of their chloro complexes. This is in accordance with the systematically "too low" concentration of chloride as compared with its input concentration. On the other hand, chloride is not likely to be removed from solution by precipitation, because geochemical calculation does not indicate saturation of any chloride-bearing mineral phase (see below).

In the last increments of percolate, however, Mg and Ca begin to be released from the sample. Thus, the overall trend of cation concentrations seems to indicate that the dominating process at the end of experiment is mineral dissolution rather than cation exchange.

Mineral dissolution. MX-80 bentonite contains a number of accessory minerals, e. g., calcite and pyrite. These minerals are likely to dissolve upon contact with Äspö solution. Mineral dissolution will tend to enhance salinity of solution, i. e., cation and anion normality.

The observed change of composition with respect to sulfate indicates that mineral dissolution happens to some degree, because sulfate is not involved in cation exchange. Geochemical modelling (EQ36) indicates no saturation whatsoever (Fig. 4.17). However, this information must be regarded with caution, because within the limited range of laboratory work funded and due to the small volumes of percolate taken at each increment, no carbonate contents could be determined. As MX-80 contains appreciable amounts of calcite it might well be possible that the percolate contains small amounts of carbonate adding to the charge balance constraint which served as base of calculation for chloride content.

Ultrafiltration. As mentioned above, compacted clays may behave like semipermeable membranes, retaining salt and rendering the percolating solution to a lower salinity. This effect would have a considerable impact on the electrical conductivity of the solution. However, the obtained data do not indicate any ultrafiltration to occur under the conditions applied.

Letting aside ultrafiltration, cation exchange and mineral dissolution will occur simultaneously within the sample. Ultimately, percolating solution should exhibit the same composition like the inflowing solution. Since this is not the case, either of both processes has not come to an end. We consider mineral dissolution as being the rate controlling process with cation exchange equilibrium establishing itself accordingly. The almost linear course of sulfate indicates a state of stationary equilibrium where some accessory mineral (perhaps pyrite) dissolve.

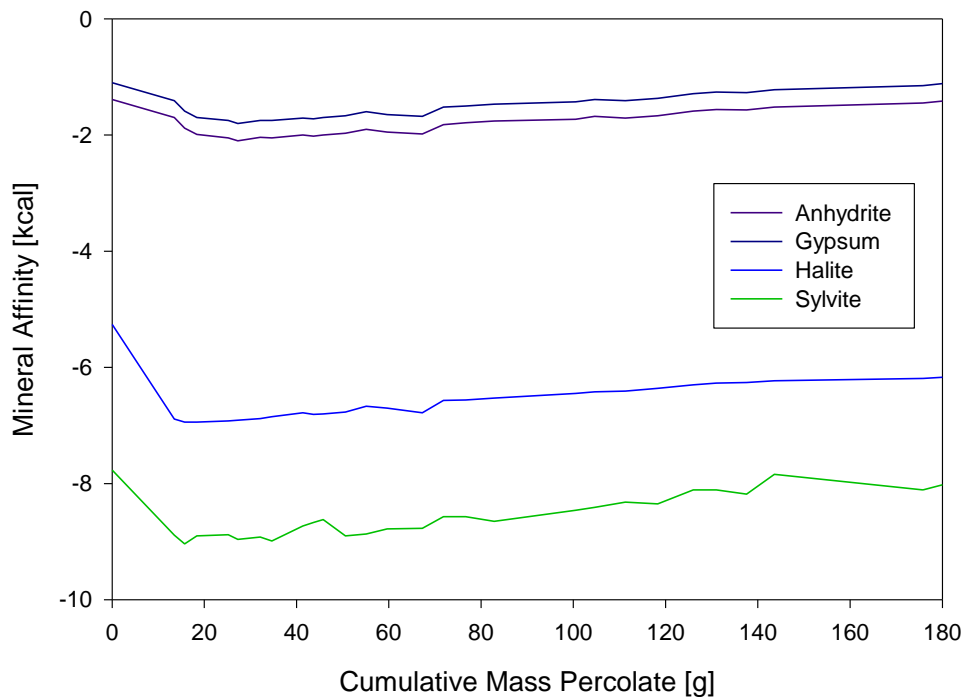


Fig. 4.17 Mineral saturation states in percolates

Approximately 30 pore volumes have penetrated the sample which is about one surface charge in terms of dissolved cations. The mass of penetrated solution exceeds the six-fold of the mass of bentonite.

This experiment was initiated by the concern that compacted bentonite could act as semipermeable membrane. By the retention of salt, electrical conductivity would have been significantly diminished. The results show that under the given conditions of solution composition, flow velocity, compaction density, layer thickness, temperature and bentonite composition no salt retention is observed. The overall salinity of solution, however, is higher than that of Äspö solution, which we assume to be the consequence of mineral dissolution. Whether this leads to a changing electrical conductivity of solution depends on the partial molar conductivity of each species present and needs to be measured in artificial solutions.

4.2 Assessment of measurement resolution

On the basis of the laboratory calibration results, modelling was performed to assess the measurement resolution which can be expected from the in-situ measurements and to support the design of the electrode arrays.

The laboratory calibrations showed that the buffer and backfill material will already have a rather small resistivity around 7 Ωm and 16 Ωm , respectively, when installed (at a water content of 12 to 13 wt%). In conjunction with the comparably high resistivity of the rock (approx. 1000 Ωm at full saturation), this may have the effect that resistivity reductions by increasing water uptake in the buffer and backfill cannot be properly detected if all electrodes for the buffer measurements are located in the rock or the electrodes in the backfill are located too close to rock. In order to clear this issue, model calculations were performed to determine optimal electrode arrangements, enabling high resistivity resolution.

Modelling was performed by calculating the expected measurement values for a given set of measurement configurations and a given inhomogeneous saturation state. Afterwards, the artificial measurement values were evaluated by inverse modelling (see Section 3.3).

4.2.1 Backfill

First model calculations used an elliptic tunnel section with an electrode configuration around the tunnel surface. The reason for an elliptic model of the tunnel (the tunnel cross section is, in fact, circular) is given by the installation procedure: The electrodes had to be installed on the backfill slope during backfill emplacement. This slope is 35° with respect to the tunnel floor. A plane through the electrodes is therefore inclined, leading to an elliptic tunnel section.

Modelling an electrode configuration around the drift surface led to insufficient results. The presence of the surrounding high-resistive rock seemed to cause a high-resistivity "ghost" anomaly in the drift centre. In order to clear up whether this result was due to insufficiencies of the employed computer code or whether it was inherent to the model and electrode configuration, two simplified rectangular models were investigated.

In both models, the tunnel has a rectangular cross section, and the electrodes (36 in total) are located along the tunnel surface. In the first model, there is no surrounding rock, which means the backfilled tunnel is isolated. In the second model, a highly resistive rock (1000 Ωm) surrounds the tunnel. The drift itself consists of a lower "wet" backfilled part (2 Ωm) and an upper "dry" backfilled part (16 Ωm). Modelling was performed by calculating artificial measurement results from the input model and afterwards performing an inversion of the "measured" data.

Figure 4.18 shows the first input model (left) and the corresponding inversion result (right). Obviously, the input model is well reconstructed by the inversion algorithm. The resolution is satisfying.

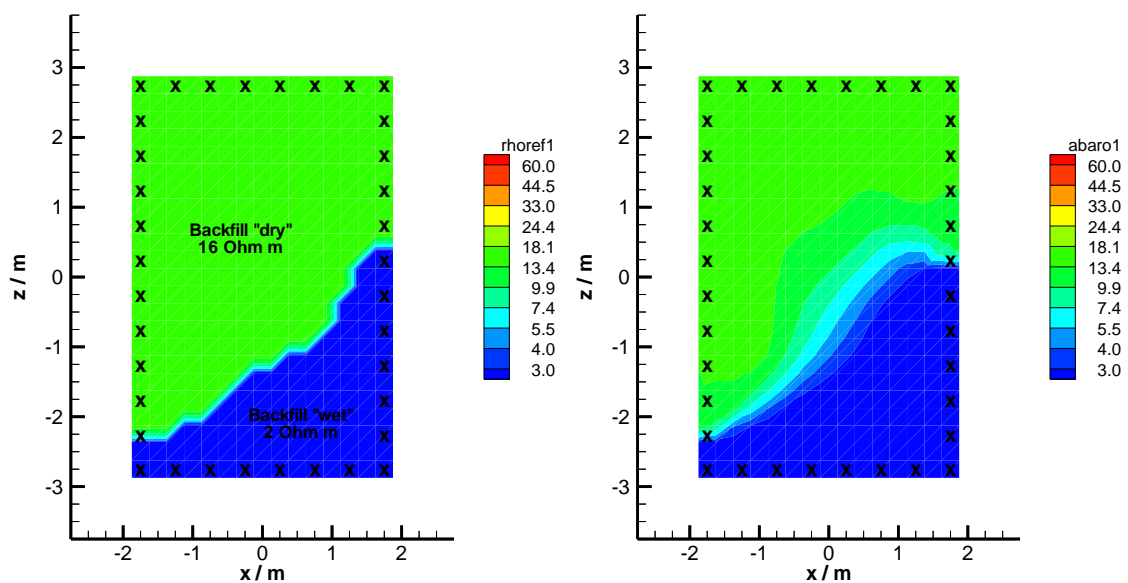


Fig. 4.18 Geoelectric modelling of the prototype repository backfill: Rectangular model without surrounding rock (left: input model, right: inversion result)

The second input model (with rock) and the corresponding inversion result are shown in Fig. 4.19. Here, the high-resistivity ghost in the tunnel centre appears again. That means the ghost does not result from a disadvantageous geometry in the original elliptic drift model, but is created as soon as the highly resistive rock is included in the model. Placing all the electrodes on the border between rock and drift will, in any case, cause this problem. Since the rock is there in reality, it cannot be left out in the model. Therefore, the only solution is an altered electrode configuration. Modelling with the elliptic drift model and different electrode configurations showed that adequate results

can be expected if a double cross of electrodes as shown in Fig. 4.20 is being installed. The "measured" resistivity change is reconstructed sufficiently well in this case.

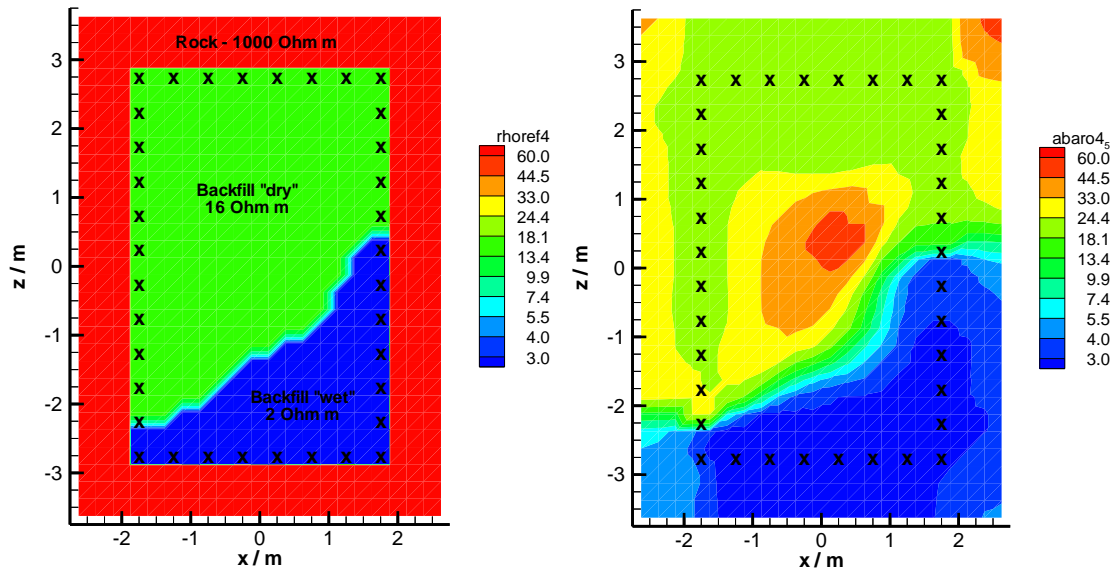


Fig. 4.19 Geoelectric modelling of the prototype repository backfill: Rectangular model with surrounding rock (left: input model, right: inversion result)

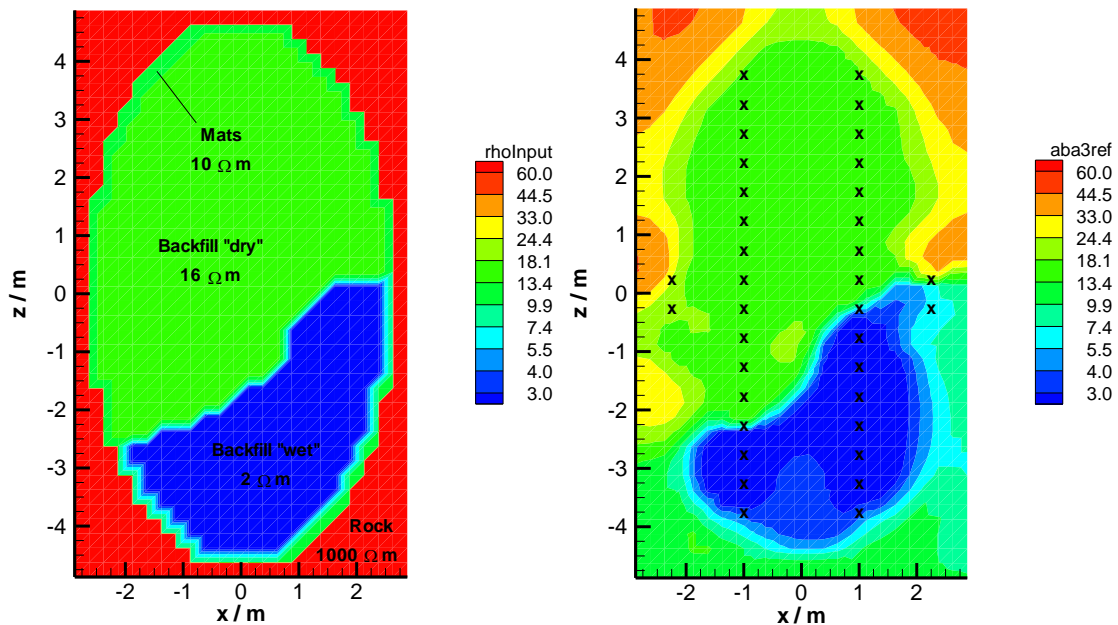


Fig. 4.20 Geoelectric modelling of the prototype repository backfill: Elliptic drift model with surrounding rock (left: input model, right: inversion result); "double cross" electrode arrangement (x = electrode locations)

4.2.2 Buffer

Various models were investigated in order to determine the most adequate electrode arrangement for the buffer. The first model used the originally planned arrangement of four electrode chains located outside the buffer in the rock. This led to completely insufficient results for the buffer. Further modelling included an additional electrode chain centred in the buffer or a chain placed horizontally on the buffer surface. While the horizontal chain gave only little improvement, the additional central chain led to better results when the buffer was modelled as homogeneous dry ($7 \Omega\text{m}$) or homogeneous wet ($4 \Omega\text{m}$). For the most interesting case, however, which incorporates a partially wetted buffer, again no satisfying results could be achieved. The modelling results with the original model, the model with an additional central electrode chain, and with a horizontal chain are shown in Fig. 4.21 to Fig. 4.23.

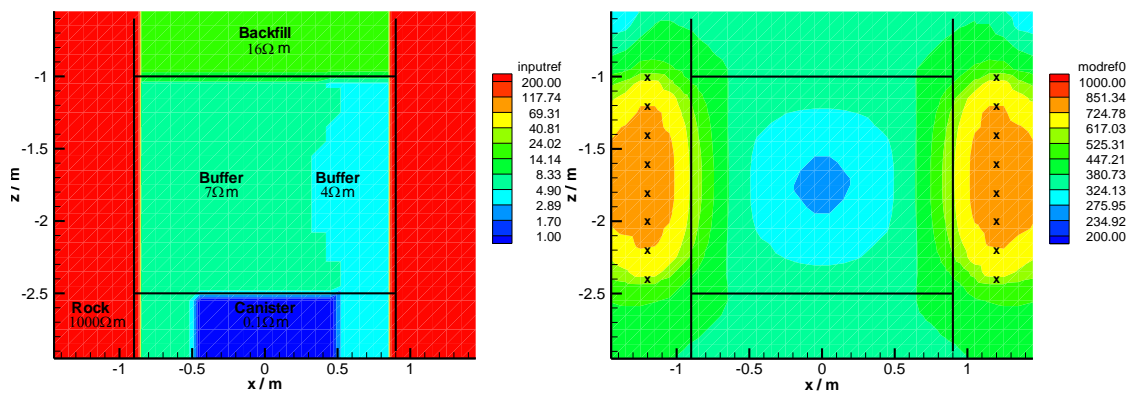


Fig. 4.21 Geoelectric modelling of the prototype repository buffer with the original electrode arrangement (left: input model, right: inversion result)

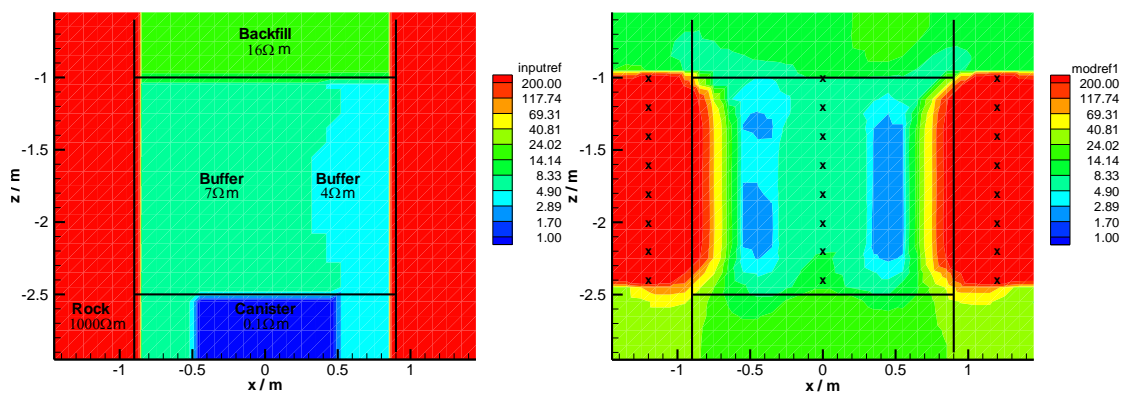


Fig. 4.22 Geoelectric modelling of the prototype repository buffer with additional central chain (left: input model, right: inversion result)

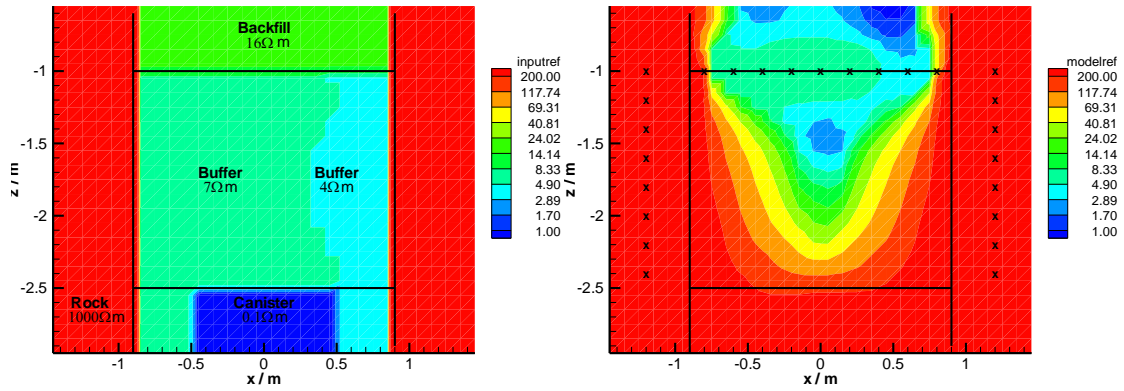


Fig. 4.23 Geoelectric modelling of the prototype repository buffer with additional horizontal chain (left: input model, right: inversion result)

In order to get a better resolution for the buffer resistivity distribution, a new electrode arrangement featuring two vertical chains in the buffer was agreed. One chain was placed near the centreline of the buffer and the other near the borehole wall. A third electrode chain in the rock at the original location was also kept.

With this electrode arrangement a new modelling series was started. Figure 4.24 to Fig. 4.26 show the results for a dry buffer, for a small wetted zone near the wall, and for an enlarged wetted zone.

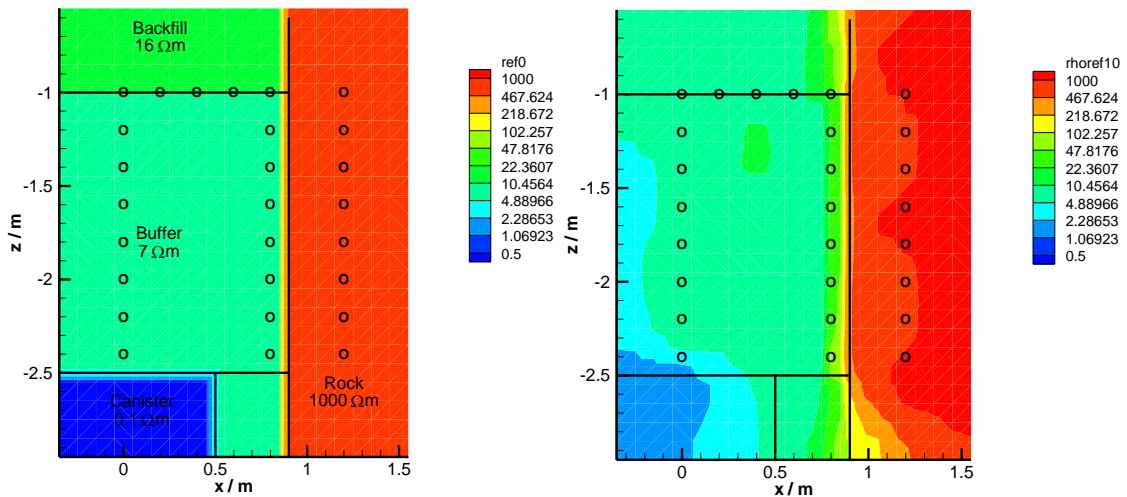


Fig. 4.24 Geoelectric modelling of the prototype repository buffer with the new electrode arrangement: dry buffer (left: input model, right: inversion result)

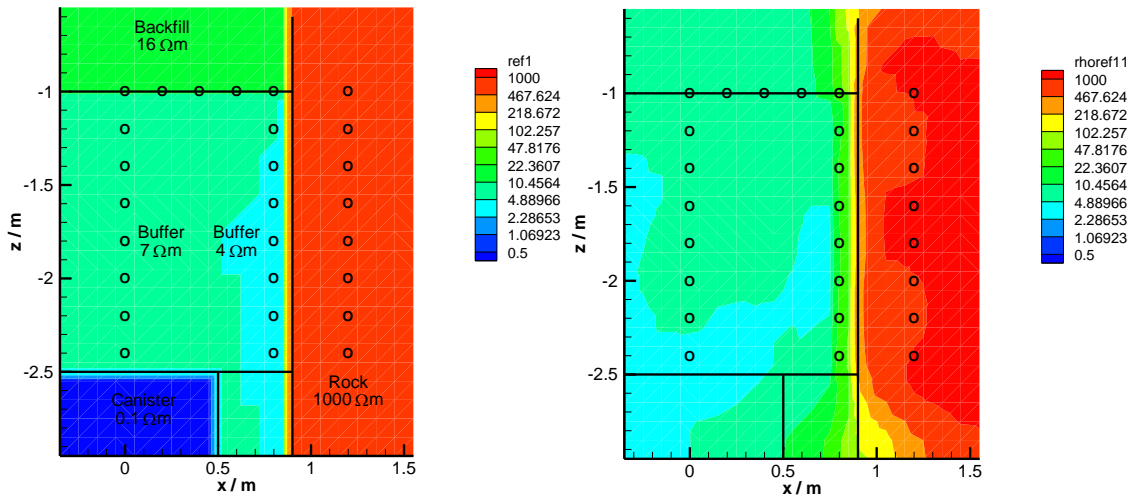


Fig. 4.25 Geoelectric modelling of the prototype repository buffer with the new electrode arrangement: partially wetted buffer (left: input model, right: inversion result)

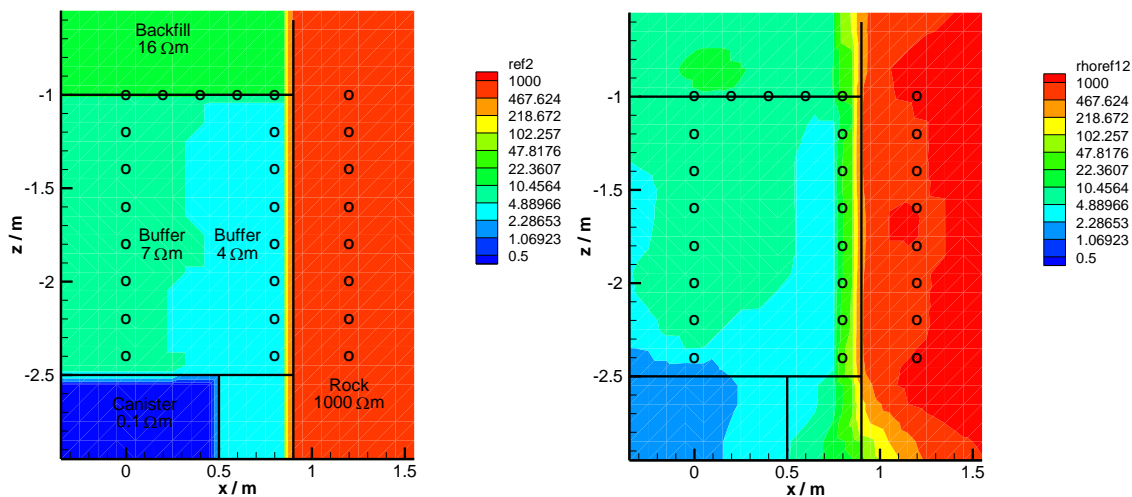


Fig. 4.26 Geoelectric modelling of the prototype repository buffer with the new electrode arrangement: enlarged wet buffer zone (left: input model, right: inversion result)

The figures show that although there are some deviations from the input model, especially at the left model border and near the heater, the buffer resistivity distribution is fitted rather well. The most interesting region near the borehole wall is modelled in a reliable way. In particular, no high or low resistivity "ghosts" are generated, as for instance in Fig. 4.22. Therefore, the new electrode arrangement appears adequate for the investigation.

5 Instrumentation

5.1 Measurement system

All geoelectric systems employed by GRS use low-frequency alternating current. Typically, 2 to 5 current cycles are injected during a single measurement. The period of a cycle is usually between 5 and 10 seconds. Such low frequencies are necessary in order to be able to treat the measurements as direct current geoelectrics; higher frequencies may result in phase differences between injected current and measured voltage. The injected current is in the range between 1 and 200 mA.

RESECS is a PC-controlled DC-resistivity monitoring system for high resolution tomography and other geoelectric applications. The RESECS measuring programme runs under MS-Windows 98. Up to 240 electrodes are separately addressable by unique decoder addresses. Any pair of electrodes might be selected as current injector. Up to six other pairs of electrodes might serve as potential electrodes for simultaneous geoelectric measurements (six channel operation). The software controlled fast switching of electrodes results in a high data acquisition rate – up to a few thousands data points per hour.

The RESECS system essentially consists of the following components:

- Resistivity meter and embedded PC
- Injection voltage supply
- Electrode decoder array
- Uninterruptable power supply

All system components are integrated in a 24 height units 19"-enclosure (see Fig. 5.1). The protection rating of the enclosure is IP54. The resistivity meter and the embedded PC are internally connected to the other components of the system. The resistivity meter is controlled by the embedded PC. Up to six potential differences are measured simultaneously. Each analogue input signal (injection current, potential differences) is supplied with a separate signal path. These signal paths are galvanically isolated from each other and from the embedded PC as well. Each one consists of high quality amplifiers (for impedance adaption, programmable gain setting and isolation),

optocouplers and DC/DC converters for the separation of power supplies. Furthermore each signal path is supplied with a DC-accurate, tunable linear phase 5th order Bessel lowpass filter. The cutoff frequencies are software selectable. The AD-converter has a resolution of 16 bit and a conversion interval of 1 ms for each channel.

The injection voltage is switched using a full bridge consisting of high voltage transistors (FET). The switching timing is defined by software. The electrode address code is created electronically by converting digital PC output to a serial function and address code.



Fig. 5.1 Geoelectric Measurement System RESECS

The embedded PC (OCTAGON SYSTEMS PC510) is supplied with 33 MByte DRAM. The PC is set to the requirements of the measuring system. Further PC components are an ethernet card and two hard disk drives. The hard disks are formatted and

partitioned. The user has access to the secondary master hard disk. The secondary master hard disk may only be removed from the system when the system is turned off.

The voltage supply, Xantrex XFR 600-2, serves as voltage supply for the injection current. This injection voltage source provides a maximum voltage of 600 V and a maximum current of 2 A. The voltage source is controlled by a serial PC interface (COM3). The switches on the rear panel of the voltage source are set to RESECS software requirements. For security reasons the output voltage is limited by software to 60 V in automatic monitoring measuring mode. In manual measuring mode the operator has full control over the output voltage.

Electrode decoders are electronic circuits used for switching relays to the measuring lines. The system has a total number of 240 addressable electrode decoders. The 18 pin electrode connectors at the rear panel of the system collect the outlets for one decoder group each. The supply voltage for the decoders is generated within the RESECS system. It is galvanically isolated from other parts of the system. The decoder and relay supply current is displayed on the ampere-meter on the front of the system.

The system is supplied with an uninterruptable power supply, Knuerr UPS Modul NP 2000c. The purpose of the UPS is to provide power to the entire measuring system for at least 60 minutes in the event of voltage breakdown or power failure. It is connected to the PC by a serial interface (COM2) and is able to monitor malfunctions of the supply voltage.

5.2 Electrode arrays and installation procedure

An overview of the electrode locations in the prototype repository is given in Fig. 5.2. There are two electrode arrays in the tunnel backfill of Section I and II, respectively, an array at the top of the buffer in deposition hole #5, and three electrode chains in boreholes in the rock between the deposition holes #5 and #6.

Differently sized electrodes were manufactured for the different measurement arrays in the Prototype Repository. According to a recommendation of the Swedish Corrosion Institute the electrode material is a stainless steel type AISI 316 (also called SS2343).

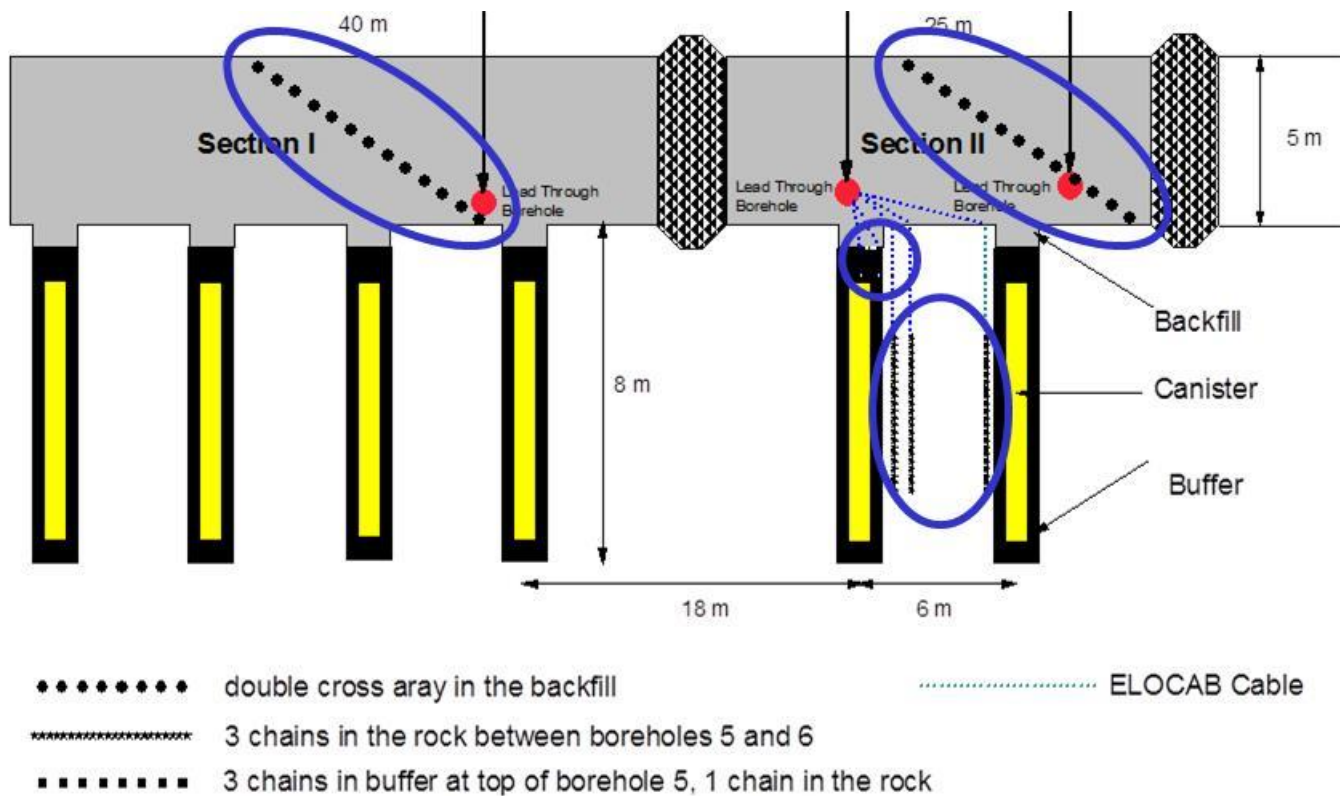


Fig. 5.2 Overview of electrode arrangements in the Prototype Repository

5.2.1 Backfill electrodes

The electrodes were manufactured according to Fig 5.3 with a diameter of 30 mm with an accuracy of ± 0.1 mm. Each electrode has a drillhole of 4 mm diameter and 10 mm depth in its neck in which the measuring wire is fastened by silver soldering. The transition from the electrode to the cable is pasted with epoxy resin and sealed with a plastic sealing which is screwed onto the electrode's neck.

All electrode chains consist of an ELOCAB multi-wire cable consisting of 37 insulated wires each filled with a swelling filler preventing migration of moisture inside the insulation sheathing (Fig. 5.4). The cables are tight against a water pressure of 10 MPa perpendicular to the cable axis and 6 Mpa along the cable axis.

The ELOCAB cables are connected pressure-tight to a GISMA-plug developed in submarine techniques (Fig. 5.5). The GISMA-plugs are pressure-tight, too, up to water pressures of 10 Mpa.

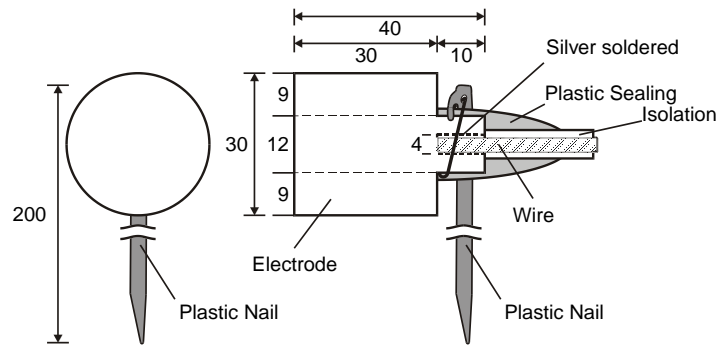


Fig. 5.3 Design of a drift electrode

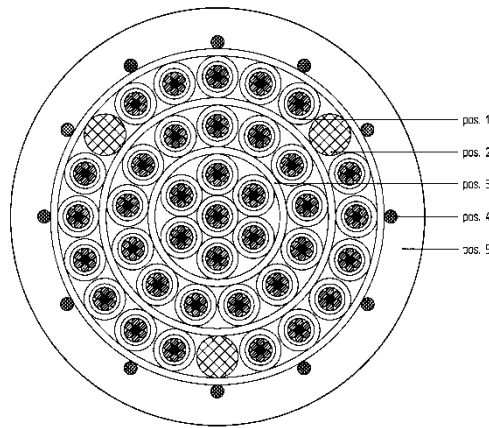
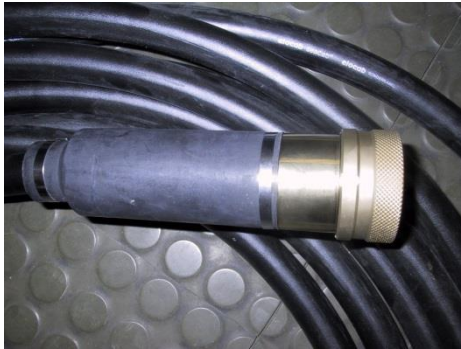
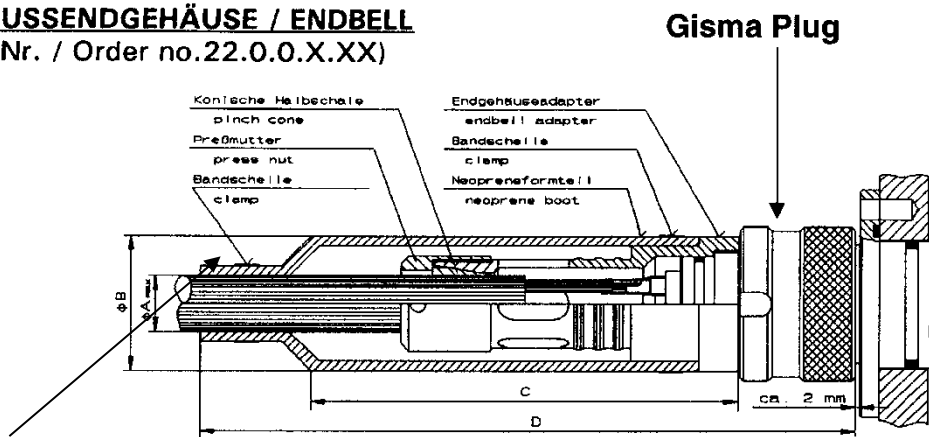


Fig. 5.4 Design of an ELOCAB cable (diameter of multi-wire cable: 27.5 mm, diameter of single wire: 2.7 mm)



VERGUSSENDGEHÄUSE / ENDBELL
(Best.Nr. / Order no.22.0.0.X.XX)



ELOCAB Multiwire Cable ERK 7673 (37 pins)

Fig. 5.5 GISMA plug

All electrode chains are of the same principle design shown in Fig. 5.6. The multi-wire part of the ELOCAB-cable reaches from the GISMA-plug to a seal from which onwards the single wires are cut to different lengths forming a chain. At each end of the single wire an electrode is fixed as described above.

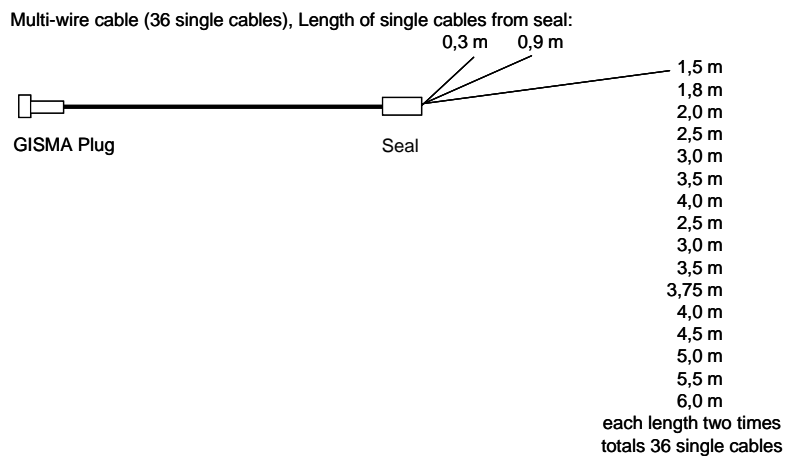


Fig. 5.6 Principle design of an electrode chain in the drift

In the backfilled drift, the chains consist simply of an ELOCAB-cable. The electrodes are fastened to the backfill by plastic nails (see also Fig. 5.3). After installation of the chain, the GISMA-plug was plugged into a GISMA socket installed at the head flange of a lead-through hole in the drift wall (Fig. 5.7).



Fig. 5.7 ELOCAB cable at head flange of a lead-through borehole

A double cross array consisting of 36 single electrodes each with a spacing of 0.5 m was installed on a 35° inclined backfill ramp above borehole #3 in Section I and a second one above deposition borehole #6 in Section II. These arrays monitor the resistivity distribution in the backfill. The array in Section I was installed from 23 to 26 October 2001 and the array in Section II from 10 to 13 June 2003. Figure 5.8 shows the installation procedure during the campaign in Section I. Details of the array dimensions are given in Fig. 5.9.

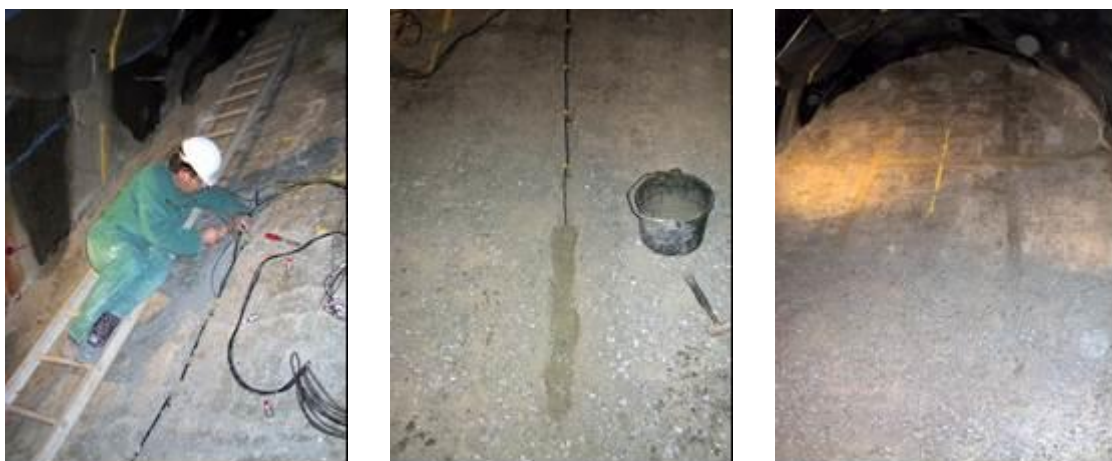


Fig. 5.8 Installation of electrode array in the backfill in Section I. Left: installation of cables in trenches, centre: trenches partially covered with fine-grained bentonite, right: completely embedded electrode array

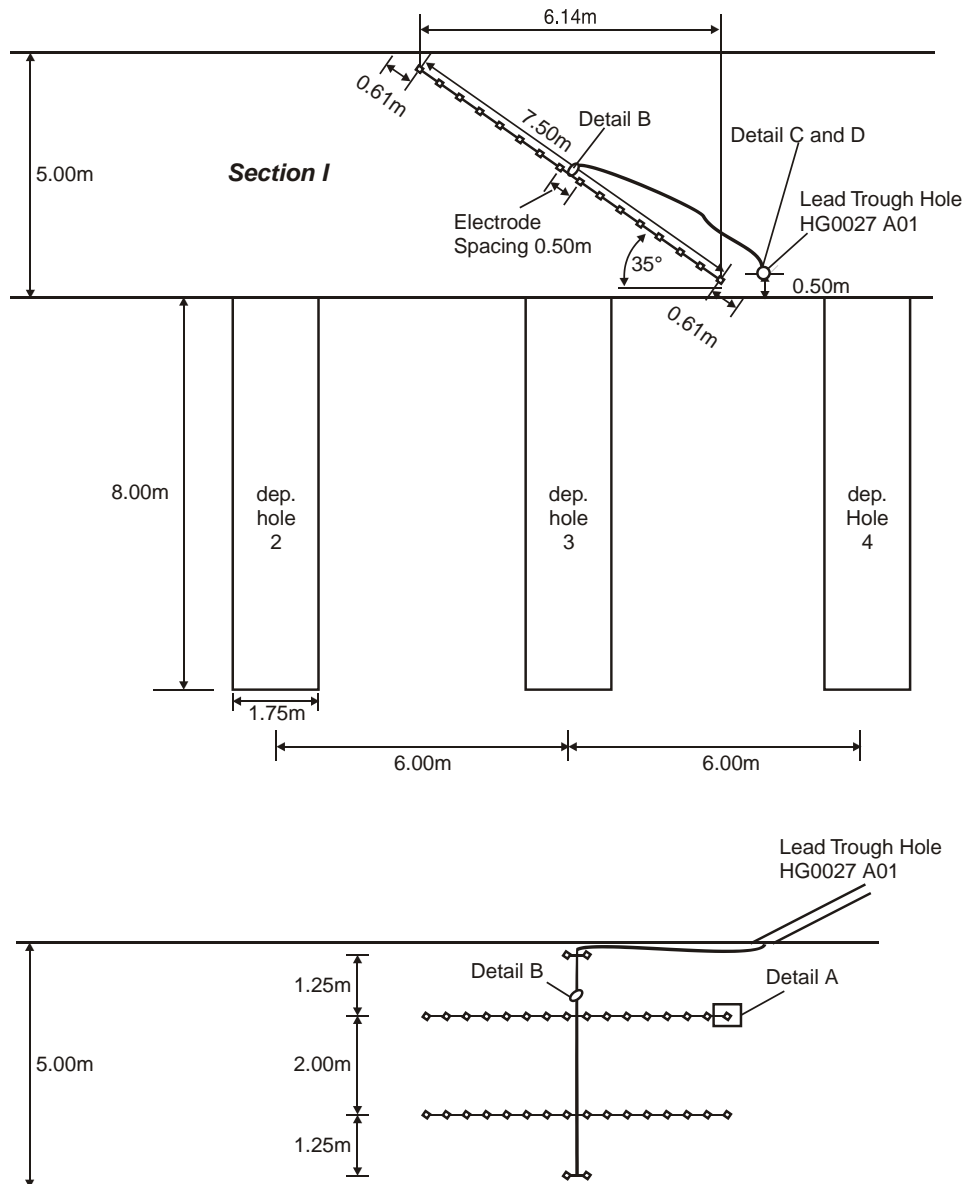


Fig. 5.9 Double cross electrode arrangement in the backfill

5.2.2 Buffer electrodes

The resistivity in the buffer at the top of deposition hole #5 is determined by dipole-dipole measurements between one horizontal electrode chain at the surface of the buffer and three vertical chains installed in the centre of the buffer, about 10 cm from the borehole wall (Fig 5.10) and outside of the borehole in the rock at 30 cm distance from the borehole wall (see Section 5.2.3). The electrode spacing is 0.1 m for the horizontal chain and 0.15 m for the vertical chains, respectively. The installation was performed from April 9 – 12, 2003. Figure 5.11 shows the installation of the electrode chain in the centre of the buffer. The complete arrangement is shown in Fig. 5.12.

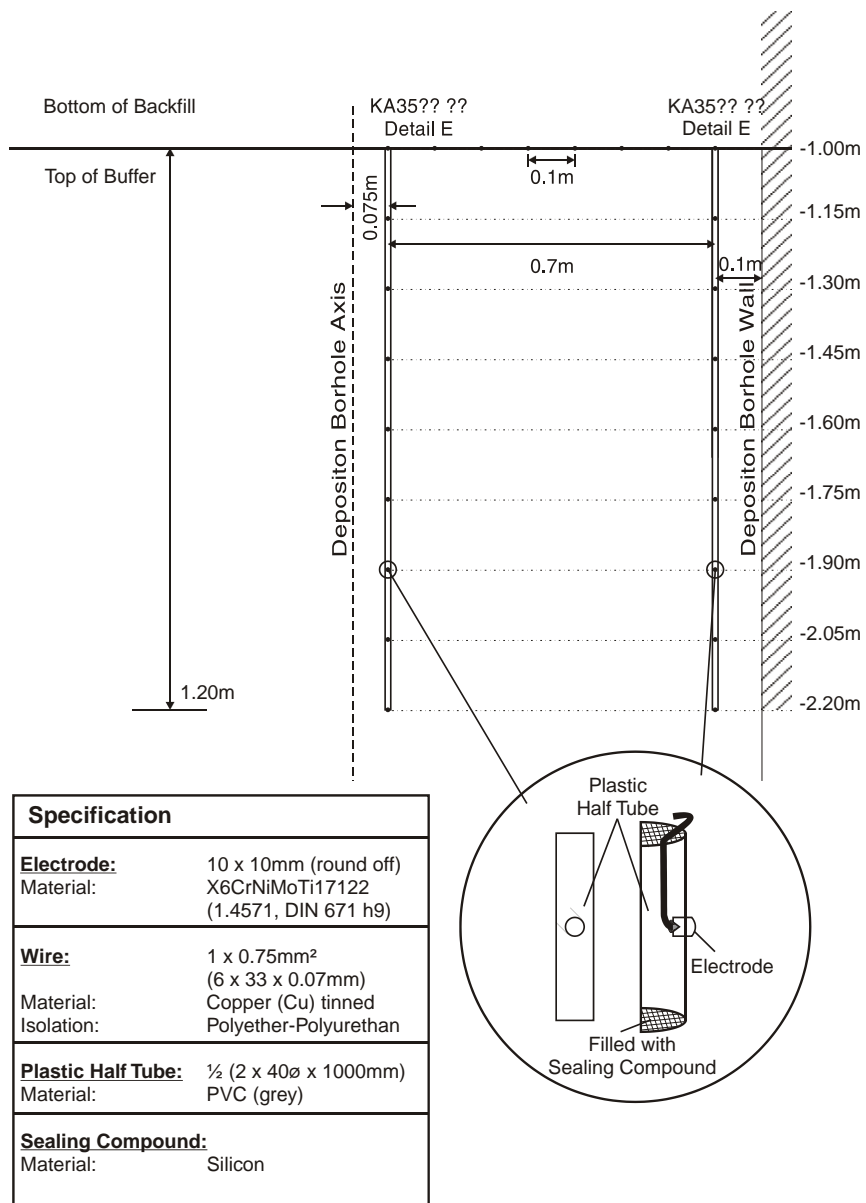


Fig. 5.10 Electrode chains at top of deposition hole #5



Fig. 5.11 Installation of electrode chain in the buffer at top of borehole 5

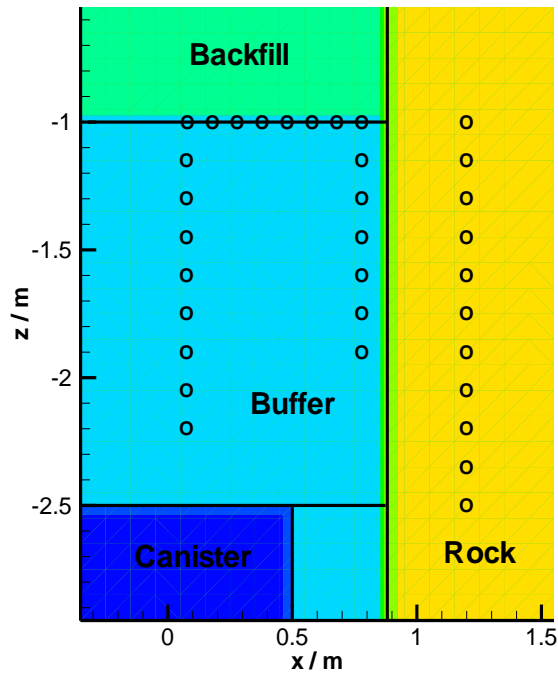
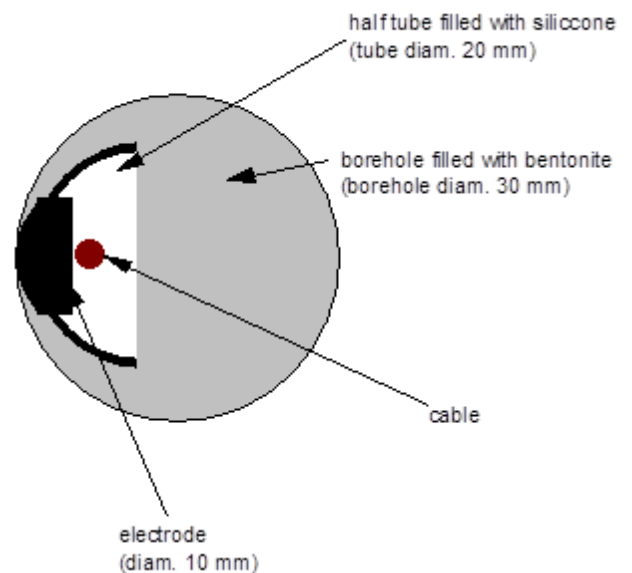


Fig. 5.12 Arrangement of electrodes in the buffer at the top of deposition hole #5 and in the adjacent rock (o = electrodes)

The electrode chains in the buffer boreholes (Fig. 5.13) consist of an ELOCAB cable with the single wires soldered to 10 mm electrodes which are fixed in the wall of a Plexiglas half tube.



a) Test block of bentonite and mock-up electrode chain



b) Horizontal cross section through buffer borehole

Fig. 5.13 Design of electrode chain in the buffer

The single wires connected to the electrodes are sealed in the half tube with silicone and guided vertically upwards out of the buffer. The electrodes were pressed against the buffer by filling the remaining volume of the borehole with bentonite powder produced during drilling of the borehole and compacting the bentonite as far as achievable to the design density of 1.66 g/cm³ by stamping with a stick. Filling of the borehole and compaction of the buffer was made in several steps with small portions of material in order to control the density of the compacted material over the whole borehole length. After installation in the buffer, the GISMA plug of the cable was plugged into the respective GISMA socket at the drift wall.

5.2.3 Rock electrodes

The resistivity distribution in the immediate vicinity of two of the deposition boreholes is monitored with three electrode chains of 30 electrodes each installed in vertical boreholes in the rock between deposition holes #5 and #6 (Fig. 5.2). An additional 12 electrodes are installed in the borehole close to deposition hole #5 at lower depth. These are used for buffer monitoring (see Section 5.2.2).

The electrode chains in the rock (Fig. 5.14) also consist of an ELOCAB cable with the single wires soldered to 10 mm electrodes which are fixed to a plastic stick inserted into the borehole in the rock. To get proper contact of the electrodes to the rock the boreholes are grouted with a special cement/crushed rock mixture. After installation in the borehole, the GISMA-plug of the cable is plugged into the respective GISMA socket at the drift wall.

Installation was performed from January 28 to February 1, 2002. Figure 5.15 shows the insertion of an electrode chain into a measuring borehole in the rock. The green tube for grouting the borehole is removed during the grouting procedure.

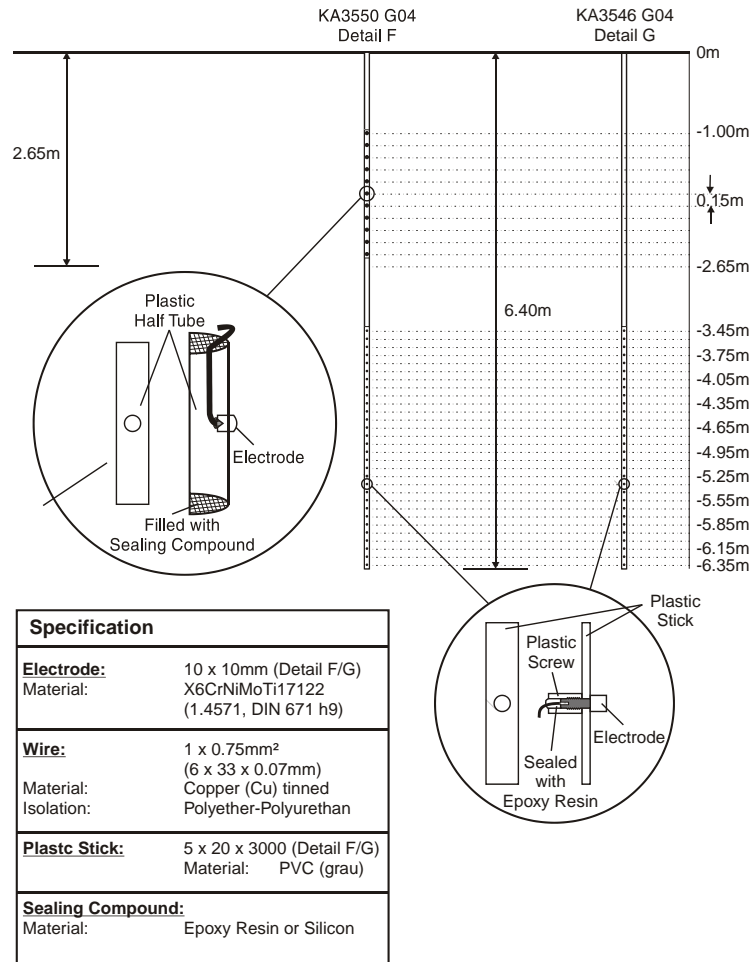


Fig. 5.14 Design of electrode chains in the rock (note the additional 12 electrodes for buffer monitoring at the upper part of the left-hand borehole)



Fig. 5.15 Insertion of an electrode chain into a measuring borehole in the rock between deposition hole #5 and #6 in Section II

6 In-situ measurements

The geoelectric measurements in the backfill and in the buffer were performed as dipole-dipole measurements leading to tomographic images, while in the boreholes in the rock profile measurements were performed. Measurements were performed on a daily basis, evaluations were done first on a quarterly, later on a semi-annual or annual basis. In case of unexpected results, additional evaluations were possible. In this section, results of the geoelectric in-situ measurements are presented. Only an excerpt of the available tomograms is shown for clarity.

6.1 Backfill Section I

The array in the backfill in Section I was the first one to be installed. Measurements started in October 2001. A series of tomograms taken between October 2001 and May 2007 is shown in Fig. 6.1.

The initial resistivity value of the backfill in October 2001 is about 10 to 14 Ωm corresponding to a water content of 13 to 14 %. In the lower part of the backfill the resistivity is somewhat higher, which is due to a lower density of the backfill near the floor (a consequence of the installation and compaction procedure). From then on, the resistivity decreased continuously, starting near the drift walls and progressing into the drift centre. From 2004 on, a very homogeneous resistivity distribution with values below 5 Ωm was reached; in May 2007 the resistivity was below 2.8 Ωm everywhere, corresponding to a water content of 21 – 22 %.

There has, however, also been a slight temperature rise in the tunnel (to maximal 32 °C) which may cause an additional resistivity decrease. This is limited, however, to less than 1 Ωm (Fig. 4.6), which means water content may be lower by 0.5 to maximal 1 %.

The water uptake from the tunnel walls and the lower saturation in the centre was also confirmed by suction measurements performed by Clay Technology /GOU 03/.

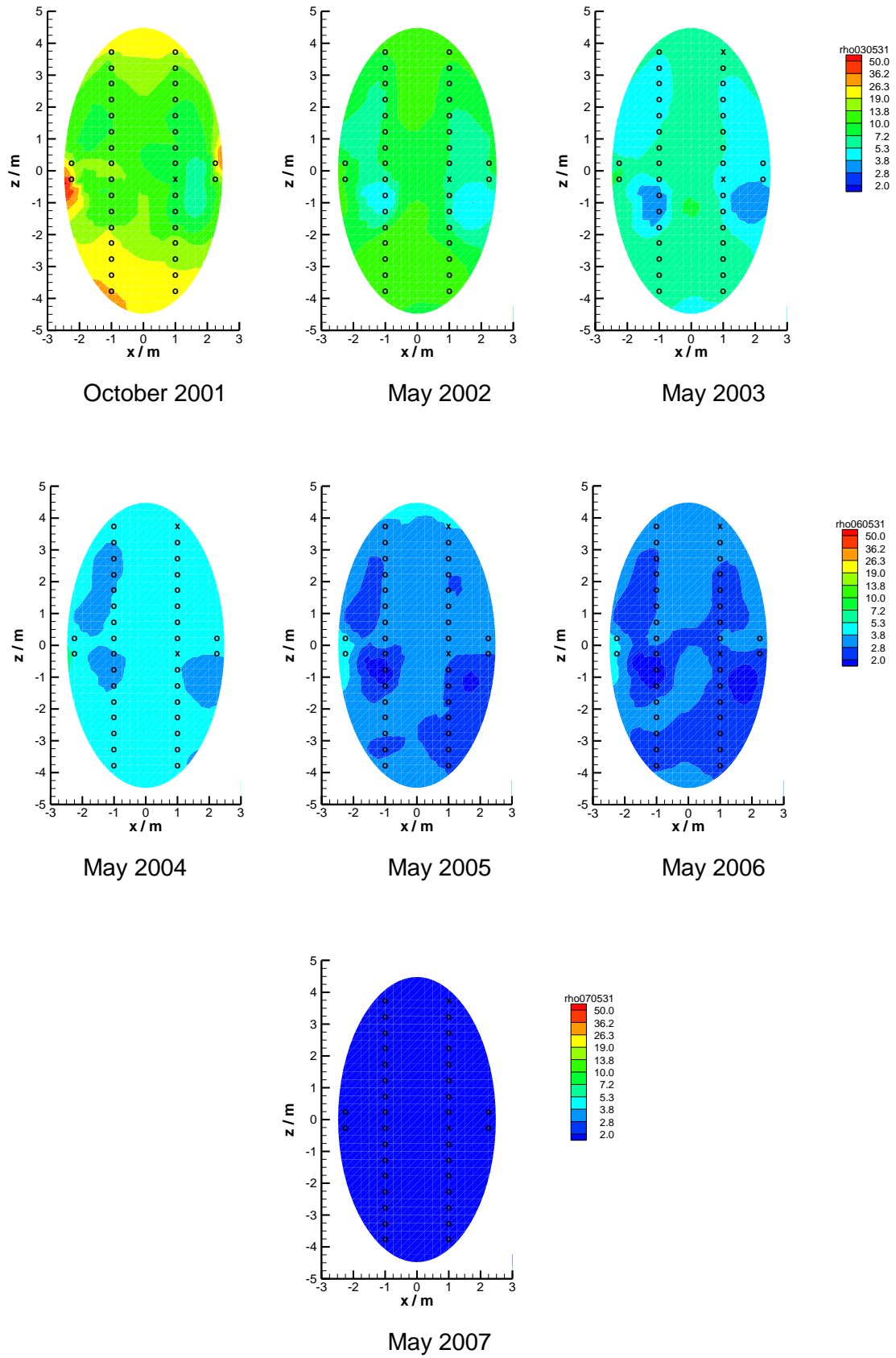


Fig. 6.1 Geoelectric tomograms of the backfill in Section I – 2001 – 2007

Besides the overall trend, minor changes in the tomograms from month to month are visible near the edges of the gallery, especially a light blue area on the right side of the tomograms is more or less pronounced. These are no real anomalies, but are caused by the fact that inaccuracies in the measurements can lead to the accumulation of "ghost" anomalies in areas of lower sensitivity. The areas of lower sensitivity are typically the edges of the model. In case of the blue area on the right side of the tomograms, the sensitivity is more reduced because one of the electrodes (marked with an "x" in the tomograms) is not active, as its cable broke after installation during backfilling.

On May 2, 2003, the upper right electrode (also marked with an "x" in the tomogram from May 31, 2003) was lost. The reason is probably a cable failure. It is not clear whether this was a corrosion effect.

The tomogram of May 2007 shows that the resistivity was below $2.8 \Omega\text{m}$ everywhere in the backfill then. To get more detailed information, the tomograms of Fig. 6.2 show the resistivity distributions since May 2007 in a different scale. Resistivity was in fact below $2 \Omega\text{m}$ (corresponding to a water content above 25 % and thus full saturation) in all of the backfill during 2007, with the values near the walls being slightly lower than in the centre. From 2008 on, however, resistivity seems to have increased again slightly. The respective tomograms show a slight increase in the entire cross section and a centre of elevated resistivity above $5 \Omega\text{m}$ near the tunnel roof. The electrodes affected by the resistivity increase are those located close to the tunnel roof – the injected current is by two orders of magnitude lower than at the other electrodes. This becomes visible when these electrodes are neglected in the evaluation, as shown in Fig. 6.3 for an example evaluation from August 2010. The resulting resistivity distribution is very homogeneous with values around $2 \Omega\text{m}$, meaning the backfill stayed fully saturated – possibly except for a small zone very close to the tunnel roof.

A possible reason for the resistivity increase close to the roof may be the continuous pumping of water out of Section I performed to reduce the water pressure in the tunnel, which may have led to a slight desaturation or a settling of the backfill resulting in a degradation of the electrode coupling.

The geoelectric measurements in Section I were finished in 2013, the tomogram from June 24, 2013 shows the last results.

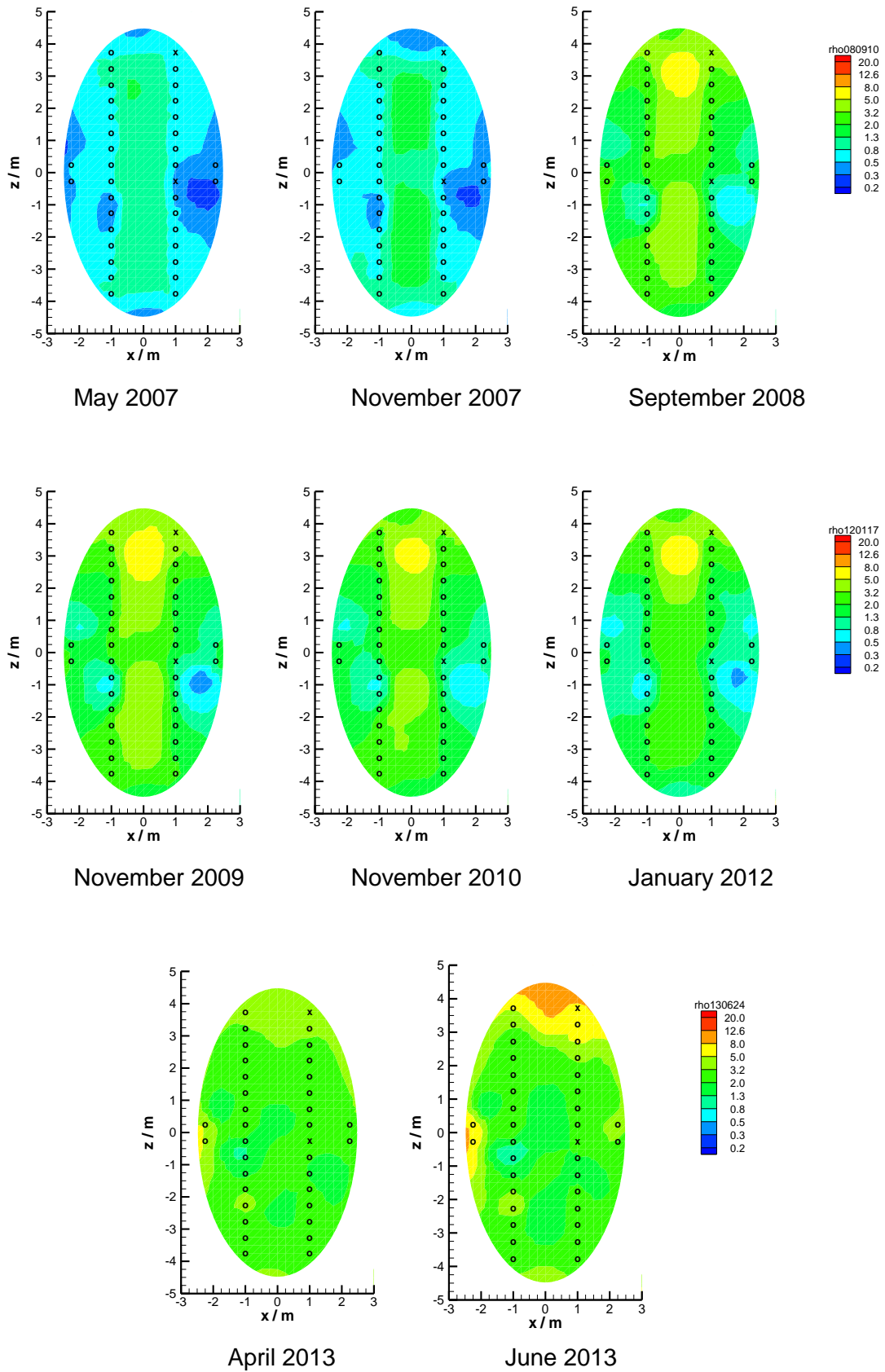


Fig. 6.2 Geoelectric tomograms of the backfill in Section I – 2007 – 2013

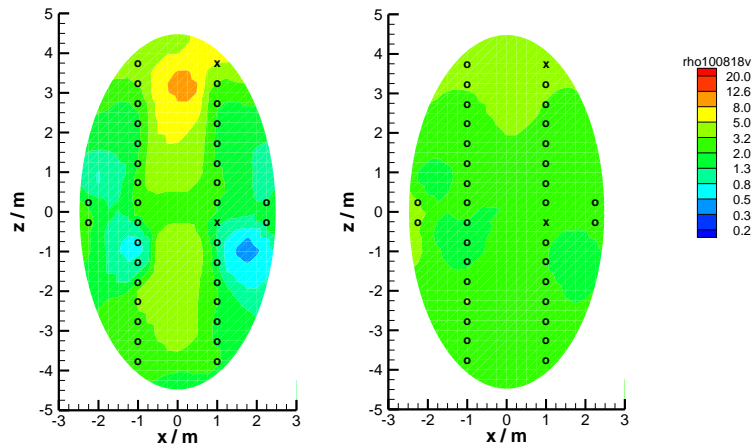


Fig. 6.3 Resistivity tomograms of the backfill in Section I, August 2010. Left: taking into account all active electrodes, right: neglecting the electrodes close to the roof

6.2 Backfill Section II

The array in the backfill in Section II was installed in June 2003. The results of the first measurement (Fig. 6.4) show a much lower resistivity than the early measurements in Section I. Obviously, the backfill had a considerably higher water content already during installation. This observation was also made during instrumentation. Resistivity decreased further from the drift walls (Fig. 6.4), similar to Section I. The central area of higher resistivity decreased continuously in size. At the end of 2009, resistivity reached values around $2 \Omega\text{m}$ everywhere in the cross section. The backfill in Section II could be considered fully saturated at that time. Afterwards, a slight increase in resistivity to a distribution comparable to the one encountered at the end of 2008 could be observed. Possibly this can also be attributed to pumping activities in the tunnel. The backfill stayed, however, largely at full saturation.

In 2011, the measurement was stopped due to the dismantling of Section II. Section II was excavated and some of the electrodes could be retrieved for inspection (see Chapter 8).

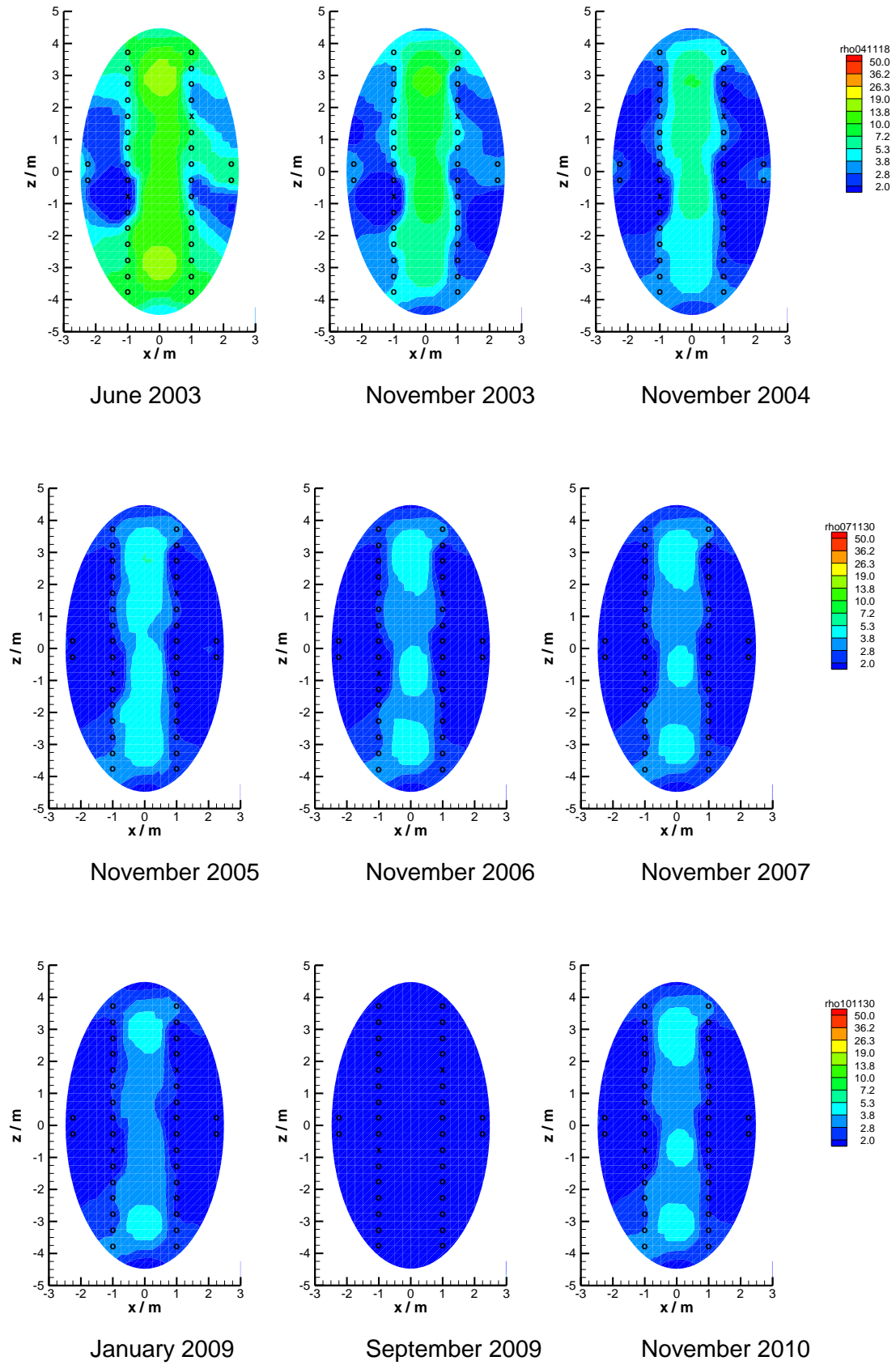


Fig. 6.4 Geoelectric tomograms of the backfill in Section II – 2003 – 2010

6.3 Buffer deposition hole #5

The tomogram of the first measurement taken in May 2003 (Fig. 6.5) shows the high resistivity (above 1000 Ωm) of the rock on the right side and the low resistivity of the buffer (below 80 Ωm). The picture is somewhat distorted by the fact that along the electrode chains the resistivity is increased compared to the undisturbed buffer. The increased resistivity along the electrode chains can be attributed to the refilling of the electrode boreholes with bentonite powder produced during borehole drilling. The density of the bentonite powder in the electrode boreholes has to be considerably lower than the bentonite blocks. It was expected that the difference would diminish with time when the buffer takes up water.

The tomograms of the following months show a progressing decrease of resistivity in the buffer. While the overall behaviour is rather clear, it is difficult to interpret buffer resistivity in terms of water content. In nearly all the buffer monitored by the array the resistivity decreased to values below 24 Ωm by November 2004 and below 13 Ωm by end of May 2005. The tomogram of November 2005 shows two high resistivity anomalies in the buffer. These are not real, but result from the fact that two electrodes were lost between September and November, 2005. The accuracy of the results is reduced by the loss of electrodes. From November 2005 on, more electrodes failed so that a tomographic evaluation was no longer possible. The injection current of the electrode pairs which were still working was still increasing, which was a hint to a further decrease in resistivity, meaning the buffer was still taking up water.

In 2011, Section II was dismantled and samples were taken from the tunnel backfill and from the buffer of the deposition holes. In particular, buffer cores containing parts of the electrode chains could be retrieved and analyzed. The reason for the electrode failure could then be attributed to cable breaks which occurred as a consequence of significant upward swelling of the uppermost buffer blocks in the range of decimetres (see Chapter 8). This elongation could not be taken by the cables. The volume increase of the buffer blocks during swelling was caused by an insufficient stiffness of the tunnel backfill above the buffer, which had not been foreseen.

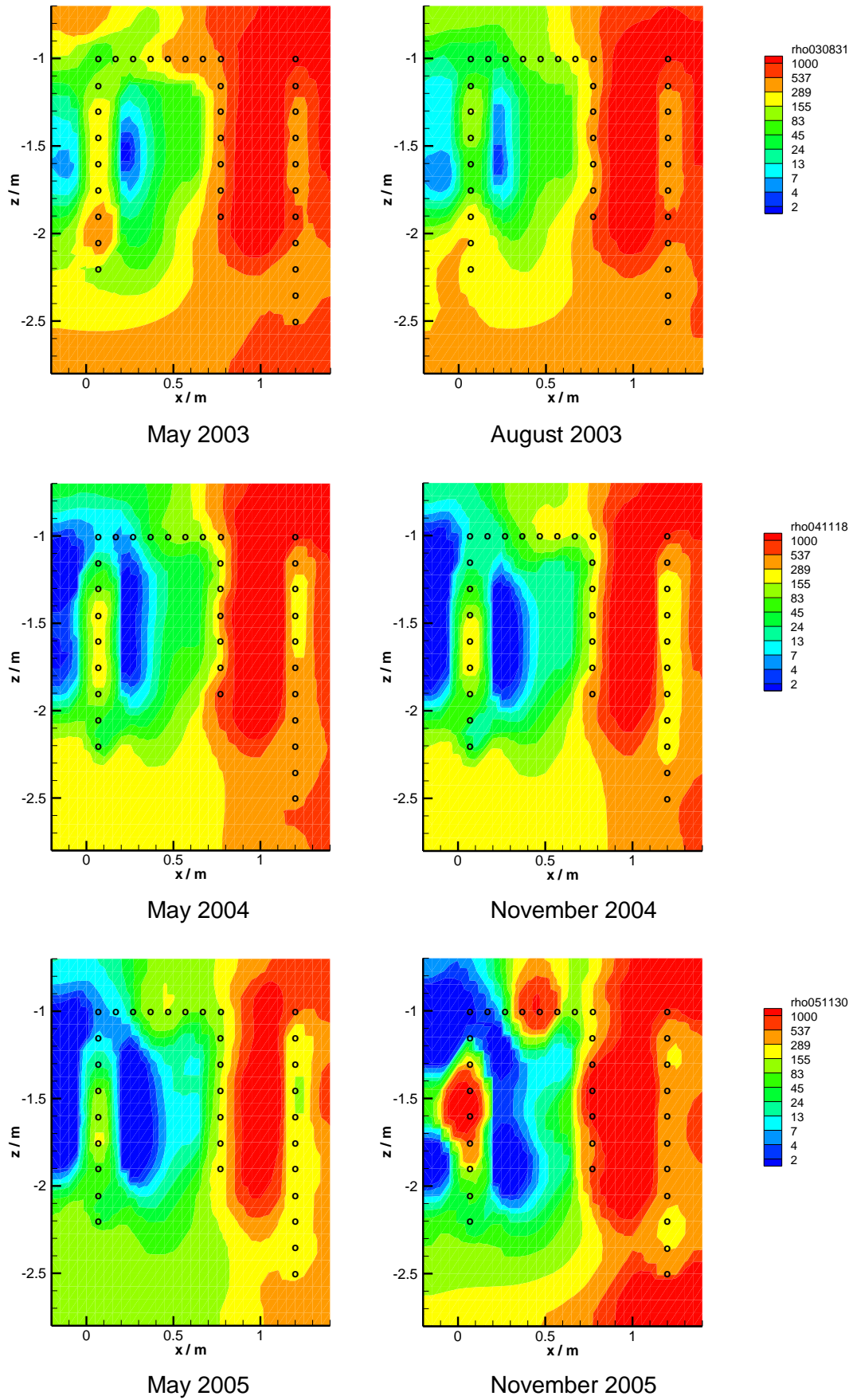


Fig. 6.5 Geoelectric tomograms of the buffer at the top of deposition hole #5

6.4 Rock Section II

In the boreholes in the rock between deposition hole #5 and #6, geoelectric profile measurements were performed. Tomographic measurements were not possible in the rock due to its high resistivity which prevented current injection between boreholes. Compared to the tomographic measurements in the backfill and the buffer, the profile measurements in the boreholes give less information about spatial resistivity distributions. The resistivity distributions along the three electrode chains installed in the rock are quite similar to each other and show no significant variation in time until April 2003. Close to the electrodes, the resistivity ranges around $200 \Omega\text{m}$. This value characterizes the water-saturated concrete used for backfilling the electrode boreholes. Further away from the boreholes, the resistivity rises to values of 2000 to $7000 \Omega\text{m}$ which is characteristic for water-saturated granite. Figure 6.6 shows the first measurement in August 2002. From spring 2003 on, there is a slight decrease in resistivity in the rock near deposition hole #5 (Fig. 6.7, left tomogram). This coincides with installation of the buffer which also stopped the pumping of water from the open deposition hole. Apparently, this had caused a slight desaturation of the rock which recovered. From February 2004, resistivity increased again. This becomes visible from May 2005 on (Fig. 6.7, 6.8, and 6.9) and might be caused by a drying of the concrete backfill of the electrode hole and possibly of the surrounding rock. Near the deposition hole #6, no such effect was detected. In 2011, the measurement was stopped due to the dismantling of Section II.

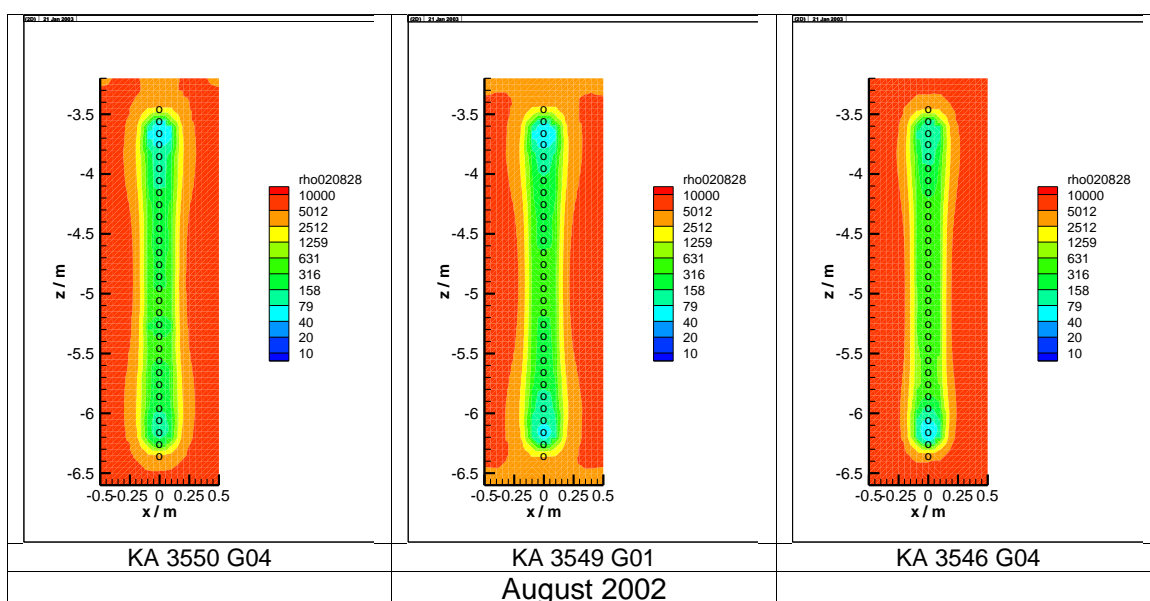


Fig. 6.6 Resistivity distribution along the electrode chains in the rock – August 2002

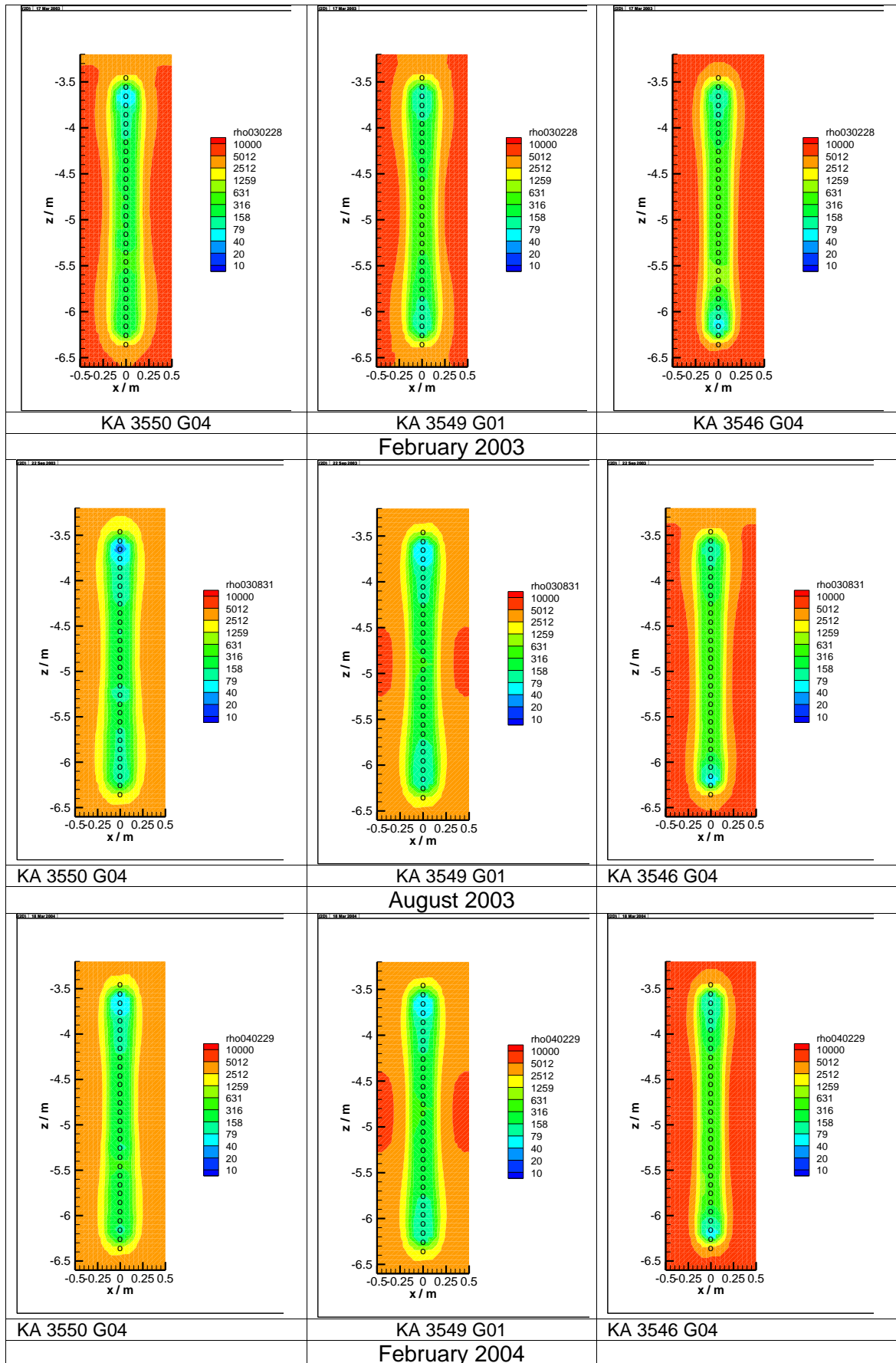


Fig. 6.7 Resistivity distribution along the electrode chains in the rock – 2003/2004

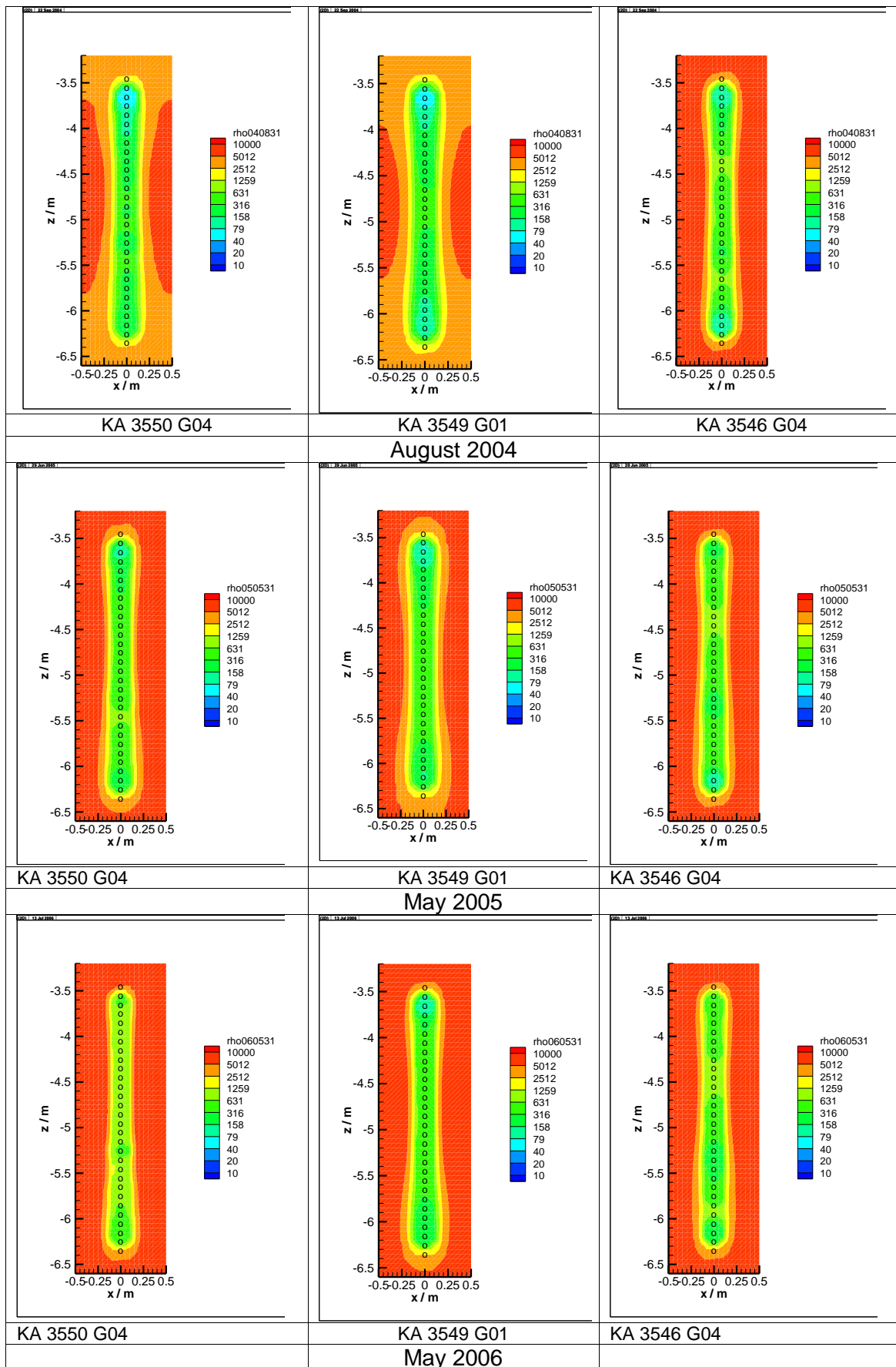


Fig. 6.8 Resistivity distribution along the electrode chains in the rock – 2004-2006

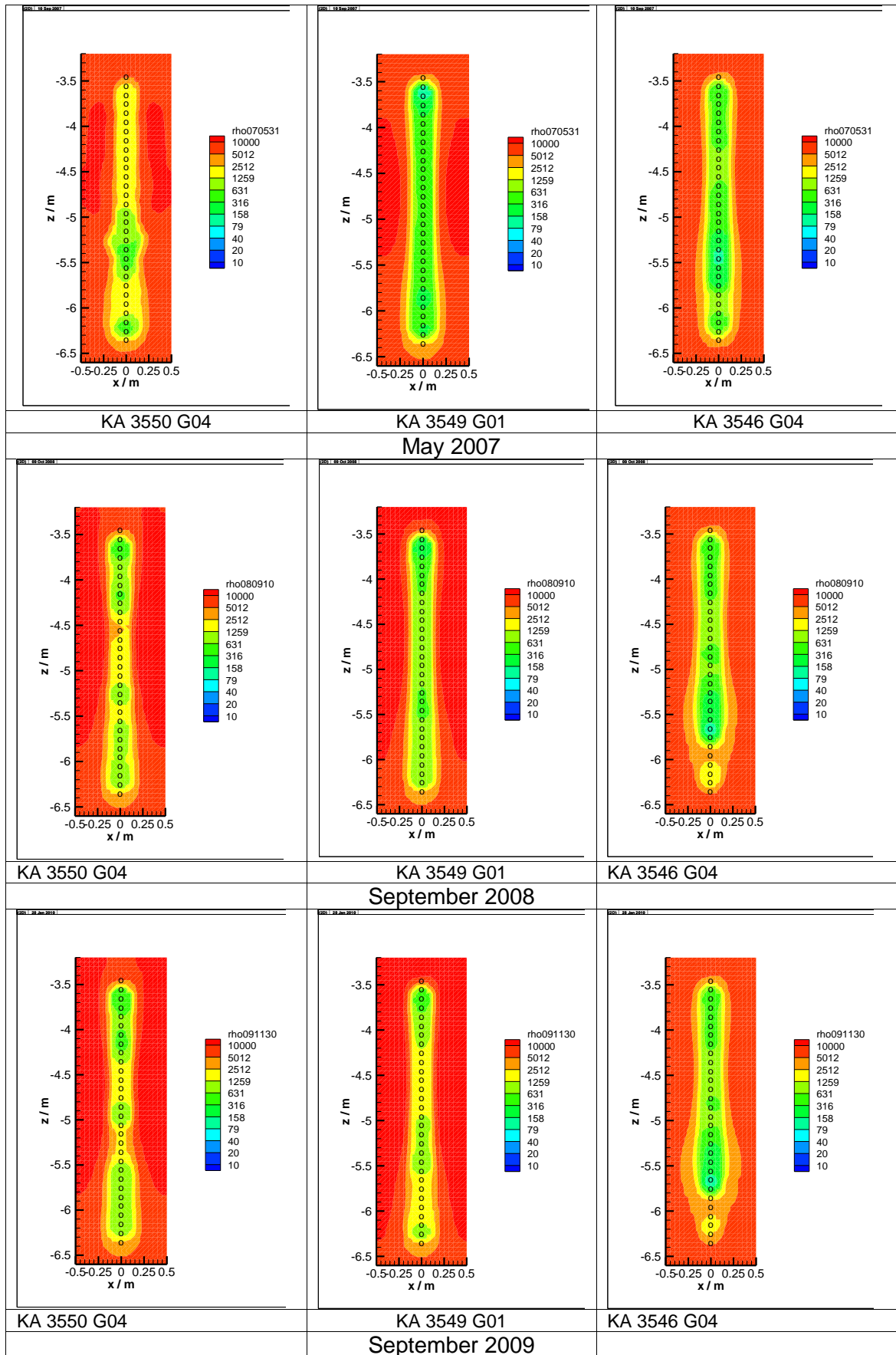


Fig. 6.9 Resistivity distribution along the electrode chains in the rock – 2007-2009

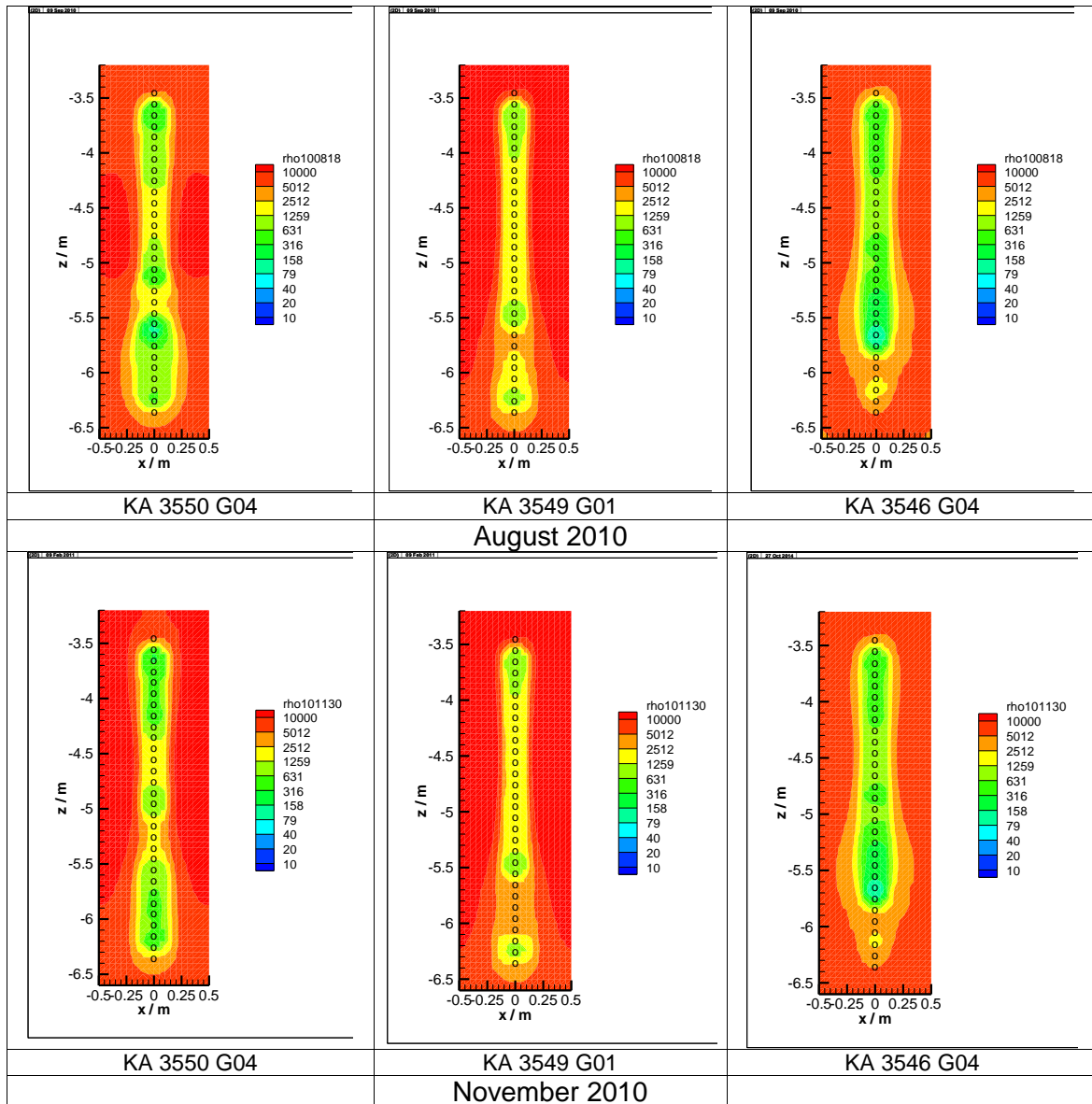


Fig. 6.10 Resistivity distribution along the electrode chains in the rock – 2010

7 Injection tests in the laboratory

The geoelectric in-situ measurements result in calculated resistivity distributions which are interpreted in terms of water content distributions. The relation between water content and resistivity, however, was determined in the laboratory on homogeneously saturated samples (see Section 4.1).

In order to show that the results of the inversion of apparent resistivities measured in situ can actually be interpreted using the laboratory calibration, injection experiments were performed in which controlled progressing water uptake in the tunnel backfill was simulated and monitored by geoelectric measurements and the water content of the non-uniform saturated backfill after injection was determined.

After a few preliminary tests to optimise experiment design and conduction, an injection test with representative backfill material, initial water content and solution was performed.

Original Prototype Repository backfill material with an initial water content of about 11 % was emplaced and compacted in a plexiglass tube of 13.6 cm inner diameter and 75 cm height equipped with four electrode profiles. After initial tomographic measurements with the original water content the tube was partially flooded from the lower end, and the geoelectric tomography measurements were repeated. Figure 7.1 shows the experimental setup and the tomograms obtained after partial flooding to a solution height of about 70 % of the tube length. After completion of the measurements the tube was dismantled, and samples of the material were taken at different heights in the tube and their water content was determined by drying and weighing.

The tomograms of Fig. 7.1 show that the saturated part of the backfill is spacially well captured. The increased resistivities close to the tube wall are geometrically induced by the curve of the tube. The cylindrical geometry cannot be considered in the model.

The saturated part of the backfill shows a resistivity of 2 – 5 Ωm corresponding to a water content of 18 – 25 %. The part of the backfill not affected by the injection stayed at a resistivity of 14 – 20 Ωm , corresponding to 11 – 13 % water content.

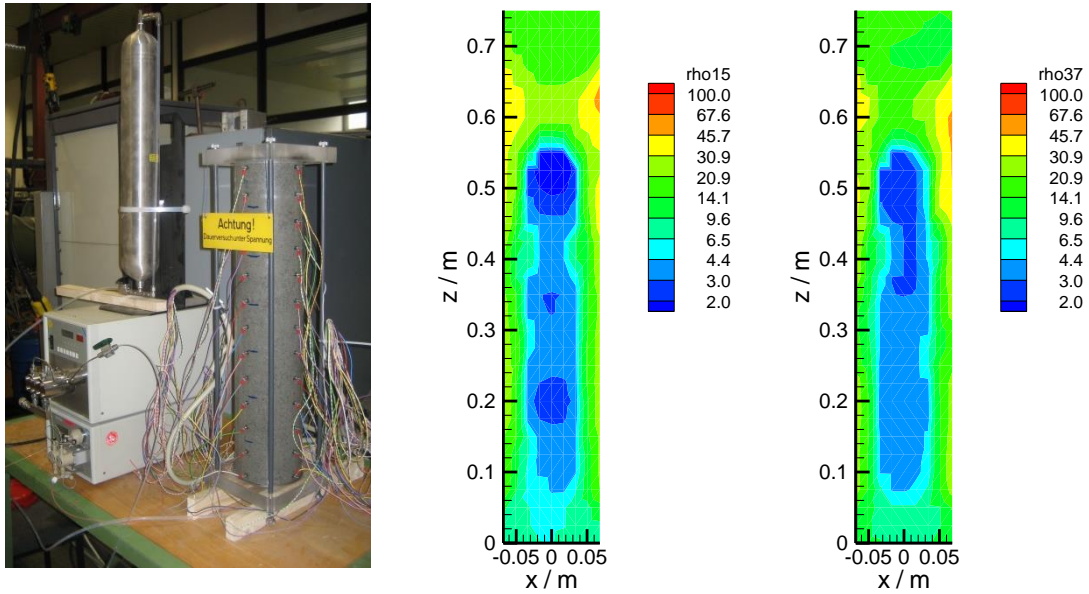


Fig. 7.1 Plexiglass tube with backfill material and electrodes (left) and resistivity tomograms obtained after flooding to 70 % height (centre and right, for two longitudinal sections)

The water content values determined on samples from the backfill obtained after dismantling ranged at 19.4 – 24.3 % for the saturated region and 10.0 – 13.8 % for the unsaturated region. This is in very good agreement with the results of the geoelectric measurements.

The experiment shows that geoelectric tomography actually yields resistivity values representative for the in-situ saturation conditions, and that interpretation of the resistivity distributions in terms of water content is valid.

8 Post-test investigations

In 2010, SKB decided to dismantle and excavate Section II of the Prototype Repository. Between 2011 and 2013, the backfill from Section II was removed from the tunnel, the buffer and the containers from the deposition holes #5 and #6 were retrieved, and various kinds of laboratory tests on a great number of samples was performed.

GRS' interest in the post-test investigations was on the confirmation of the results regarding water content distribution and especially on discovering the reason for the electrode failures in the buffer.

During excavation of Section II, a few of the backfill electrodes were retrieved. From the top of deposition hole #5, the two buffer electrode chains were overcored. Backfill electrodes and sections of the buffer cores were sent to GRS for inspection in May, 2012.

8.1 Electrode inspection

8.1.1 Backfill electrodes

Several of the electrodes installed in the backfill of Section II were retrieved during the excavation. A visual inspection showed clear signs of surface corrosion (Fig. 8.1). During more than 7 years of operation of the array there had been, however, no electrode failure of the backfill electrodes in Section II. Resistance measurements between the electrode surfaces and the connection cables showed perfect contact in all cases. Consequently, corrosion does not seem to be an issue for the backfill electrodes.



Fig. 8.1 Electrodes from the backfill in Section II showing surface corrosion

8.1.2 Buffer electrodes

Two core samples with embedded electrode chains (Fig. 8.2) were retrieved from the buffer, one from the centre and one close to the deposition hole wall. The cores had been obtained by drilling small-diameter boreholes around the electrode chain, this is the reason for the shape of the core cross section. The core shown is the one from the buffer centre.

As a first step, coupling of the electrodes to the surrounding core was tested by performing two-point current injection tests between different electrode couples. It was found that none of the electrodes had contact to the buffer core. Then, the core was sawed in axial direction (Fig. 8.3). It was found that the electrodes were nicely coupled to the buffer, but during retrieval of the electrode chain all electrodes proved to be disconnected from their cables (Fig. 8.4).



Fig. 8.2 Core section from the top central buffer of deposition hole #5 with embedded electrode chain



Fig. 8.3 Electrode chain embedded in the buffer



Fig. 8.4 Retrieved electrode chain

The reason for the cable failure is a significant upward swelling of the uppermost buffer blocks, which led to an upward displacement of the buffer top in the range of 15 centimetres which was found during the post-test investigations. The height of the two uppermost blocks increased by about 10 cm due to swelling. This elongation could not be taken by the cables. The volume increase of the buffer blocks during swelling was caused by an insufficient stiffness of the tunnel backfill above the buffer, which had not been foreseen.

There were also slight corrosion marks on the electrodes, but to a much lesser extent than on the backfill electrodes. Since the backfill electrodes never failed it is concluded that corrosion played no role for the buffer electrode failure.

8.2 Buffer water content

From both buffer cores samples were taken at different locations, as indicated in Fig. 8.5. The water content of the samples was determined by drying at 105 °C. The measured water content is shown colour coded in Fig. 8.5; the actual values are given in Tab. 8.1. All results were in the range between 21.5 wt.% and 23.7 wt.% of water. The core close to the deposition hole wall is somewhat wetter than the central core, which can be expected, since the buffer was saturated from the deposition hole wall.

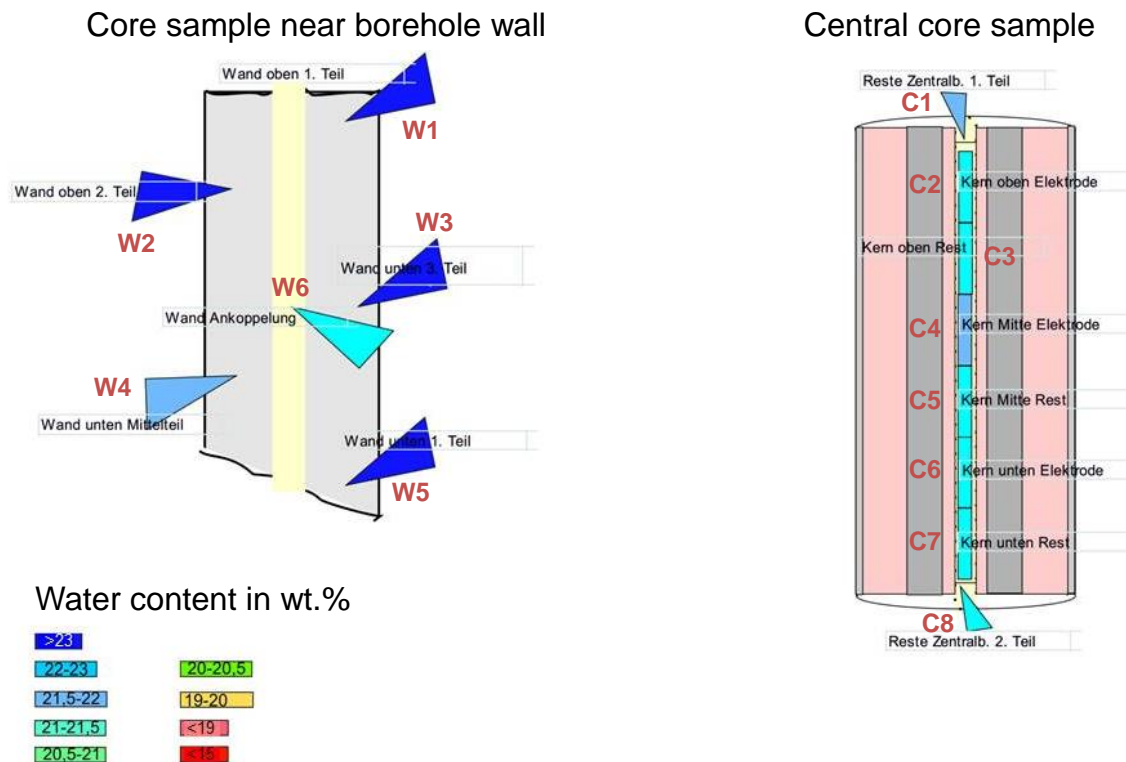


Fig. 8.5 Location of samples for water content analysis with colour coded results

Tab. 8.1 Measured water content of buffer core samples

Buffer core	Sample	Water content [wt.%]
Near borehole wall	W1	23.7
	W2	23.3
	W3	23.2
	W4	22.0
	W5	23.2
	W6	22.4
Near Centre	C1	22.0
	C2	22.7
	C3	22.7
	C4	21.5
	C5	22.3
	C6	22.2
	C7	22.2
	C8	21.8

The results are in good agreement with the water content analyses performed by Clay Technology. In Fig. 8.6, Clay Technology's results for the upper buffer of deposition hole #5 are summarized. GRS' results around 22 wt.% in the centre (marked with a light blue circle in Fig. 1.7) blend in very well, the same holds for the values around 23 wt.% close to the deposition hole wall (dark blue circle in Fig. 1.7), taking into account that the core originates from 180° azimuth. While water content was very inhomogeneous around the deposition hole perimeter, the values for 180° azimuth are in good agreement with Clay Technology's results for 205°.

9 Conclusions

Geoelectric measurements of the resistivity distribution in the tunnel backfill, the buffer on top of a deposition hole, and in the rock between two deposition holes were performed in the Äspö Prototype Repository. The measurements were started with the construction of the Prototype Repository and finished in with the dismantling of Section II in 2011; in Section I measurements were continued until 2013.

For the in-situ monitoring a commercially available automatic measuring system was employed, the electrodes, electrode coupling and wiring were designed by GRS. Laboratory calibration measurements were performed in order to be able to relate measured resistivity fields to water content distributions. Preliminary experiments and modelling were performed to make sure the electrode arrays would be well designed and the obtained results would be meaningful.

In the tunnel backfill of both Sections I and II, the progressive resaturation could be followed with good temporal and spatial resolution. In Section II, the water release from the rock takes place at a much higher rate than in Section I. Electrode design and arrangement as well as measurement method and evaluation procedure proved suitable. Only two electrodes (of 72) failed, one of them during emplacement. Post-test investigations showed that some corrosion of the electrodes occurred, but played no role for the measurements. In an additional injection experiment in the laboratory, the transferability of the calibration results on homogeneously saturated samples to inhomogeneous moisture distributions was shown. The tunnel backfill monitoring can be rated as altogether successful, delivering plausible, coherent and verifiable results.

For the monitoring of the buffer at the top of deposition hole #5, the findings are less clear. From the beginning, the resistivity distribution in the borehole was more complicated, and accordingly more effort had to be taken in the electrode array design. The first results were promising. After 2.5 years of monitoring, however, many of the electrodes failed. The post-test investigations showed that this was due to cable failure when the bentonite blocks increased in height during swelling. This swelling was not expected beforehand, the backfill above the deposition hole should have been stiff enough to prevent the uplifting of the buffer surface. The buffer electrodes were still well coupled to the buffer, and there was no sign of extensive corrosion. From that point of view, the buffer electrodes and the installation method can be considered suitable. An overall proof that the buffer array was suitable for monitoring buffer

resaturation over longer periods is, however, not possible. Water content measurements of buffer cores resulted in values around 22 wt.% in the centre and around 23 wt.% close to the deposition hole wall. These results agree perfectly with measurements performed by Clay Technology.

The electrode chains in the three boreholes in the rock performed well throughout the monitoring time of more than eight years. Electrode coupling by grouting in boreholes is standard, so this is an expected result. Although some variations in the rock resistivity was observed, the effects are not dramatic. Compared to the tomographic measurements in the backfill and the buffer, the profile measurements in the boreholes give less information about spatial resistivity distributions. Tomographic measurements were not possible in the rock due to its high resistivity which prevented current injection between boreholes.

All in all, it has been shown that geoelectric tomography is suitable for monitoring resaturation of clay-bearing sealing materials, if the measurements are carefully planned and evaluated. Special care has to be taken with regard to the possibility of mechanical damage due to swelling.

Acknowledgements

The authors would like to thank the German Bundesministerium für Wirtschaft und Energie (Federal Ministry of Economics and Energy, BMWi) for the support given to the project under the contract numbers 02E9279 and 02E9944. Part of the work was also co-funded by the Commission of the European Communities (CEC) under contract No. FIKW-CT2000-00055, which is gratefully acknowledged.

Special thanks go to the colleagues of the partner organisations, especially SKB and Clay Technology, for their support and aid.

References

- /BEN 84/ Benzel, W. M.; Graf, D. L. (1984): Studies of smectite membrane behaviour: Importance of layer thickness and fabric in experiments at 20°C, *Geochim. Cosmochim. Acta* (48), 1769-1778.
- /DAH 98/ Dahlström, L.-O. (1998): Testplan for the Prototype Repository, Progress report HRL-98-24, Äspö Hard Rock Laboratory, SKB, Stockholm.
- /DEM 88a/ Demir, I. (1988): Studies of smectite membrane behaviour: electrokinetic, osmotic and isotopic fractionation at elevated pressures, *Geochim. Cosmochim. Acta* (52), 727-737.
- /DEM 88b/ Demir, I. (1988): The interrelation of hydraulic and electrical conductivities, streaming potential, and salt filtration during the flow of chloride brines through a smectite layer at elevated pressures, *Journal of Hydrology* (98), 31-52.
- /DIN 89/ DIN 18121-1: Baugrund, Untersuchung von Bodenproben - Wassergehalt-Teil 1: Bestimmung durch Ofentrocknung, Normenausschuss Bauwesen (NABau) im DIN Deutsches Institut, Normen e.V., April 1989.
- /DRE 63/ Dresner, L.; Kraus, K. A. (1963): Ion exclusion and salt filtering with porous ion-exchange materials, *J. Phys. Chem.* (67), 990-996.
- /FEC 01/ Fechner, T. (2001) SensInv2D-Manual, Geotomographie, Neuwied.
- /GOU 03/ Goudarzi, R., Börgesson, L. (2003): Äspö Hard Rock Laboratory – Prototype Repository – Sensors data report (Period: 010917-030301), IPR-03-23, Svensk Kärnbränslehantering AB (SKB), Stockholm.
- /HAN 73/ Hanshaw, B. B.; Coplen, T. B. (1973): Ultrafiltration by a compacted clay membrane. II - Sodium ion exclusion at various ionic strengths, *Geochim. Cosmochim. Acta* (37), 2311-2327.

- /ISH 96/ Ishiguro, M.; Matsuura, T.; Detellier, C. (1996): A study on the solute separation and the pore size distribution of a montmorillonite membrane, *Sep. Sci. Technol.* (31/4), 545-556.
- /JOH 79/ Johnson, K. S. (1979): Ion association and activity coefficients in electrolyte solutions, Ph. D. Thesis, Oregon State University.
- /JOH 81/ Johnson, K. S.(1981): The calculation of ion pair diffusion coefficients: a comment, *Mar. Chem.* (10), 195-208.
- /JOH 11/ Johannesson, L.-E., Grahm, P. (2011): Prototype Repository – Status of field activities, presentation during the project meeting at Äspö, November 2011.
- /KEM 63/ Kemper, W. D.; Evans, N. A. (1963): Movement of water as affected by free energy and pressure gradients III. Restriction of solutes by membranes, *Soil Sci. Soc. Am. Proc.* (27), 485-490.
- /KEM 64/ Kemper, W. D.; Maasland, D. E. L. (1964): Reduction in salt content of solution on passing through thin films adjacent to charged surfaces, *Soil Sci. Soc. Am. Proc.* (28), 318-323.
- /KEM 95/ Kemna, A. (1995): Tomographische Inversion des spezifischen Widerstandes in der Geoelektrik, Master Thesis, Universität Köln.
- /KHA 73/ Kharaka, Y. K.; Berry, F. A. F. (1973): Simultaneous flow of water and solutes through geological membranes - I. Experimental investigation, *Geochim. Cosmochim. Acta* (37), 2577-2603.
- /KHA 76/ Kharaka, Y. K.; Smalley, W. C. (1976): Flow of water and solutes through compacted clays, *Am. Assoc. Petr. Geol. Bull.* (60/6), 973-980.
- /MAR 48/ Marshall, C. E. (1948): The electrochemical properties of mineral membranes. VIII The theory of selective membrane behaviour, *J. Phys. Chem.* (52), 1284-1295.

- /SCH 73/ Schick, R. and Schneider, G. (1973): Physik des Erdkörpers – Eine Einführung für Naturwissenschaftler und Ingenieure, Ferdinand Enke Verlag Stuttgart.
- /SCH 82/ Schopper, J. R.: Electrical conductivity of rock containing electrolytes. In: Landold-Börnstein, Numerical Data and Functional Relationships in Science and Technology. New Series edited by K.-H. Hellwege, Groupe V: Geophysics and Space Research, Volume 1, Physical properties of Rocks, subvolume b, edited by G. Angenheiser., Springer-Verlag Berlin, Heidelberg, New York 1982.
- /SER 84/ Serra, O.: Fundamentals of well-log interpretation. 1. The acquisition of well logging data. (Development in petroleum science 15A), Elsevier; Amsterdam – Oxford – New York – Tokyo 1984).
- /SKB 11/ Äspö Hard Rock Laboratory – Planning Report for 2011, International Progress Report IPR-10-19, Svensk Kärnbränslehantering AB, February 2011.
- /SPO 89/ Sposito, G. (1989): The Chemistry of Soils, Oxford University Press.
- /SVE 00/ Svemar, C., Pusch, R. (2000): Äspö Hard Rock Laboratory – Prototype Repository, Project description FIKW-CT-2000-00055, International Progress Report IPR-00-30, Svensk Kärnbränslehantering AB, November 2000.
- /ZIM 01/ Zimmer, U. (2001): In: Twophaseflow-Experiment in fractured crystalline rock, GRS-report, to be published.

List of figures

Fig. 1.1	Overview of the Äspö Prototype Repository (modified after /SKB 11/)	1
Fig. 3.1	Principle configuration of a dipole-dipole measurement	8
Fig. 4.1	Schematic view of the resistivity measurement cell for compacted MX-80 samples	13
Fig. 4.2	Schematic experiment layout for the determination of sample resistivity	14
Fig. 4.3	Resistivity of compacted MX-80 samples and original ÄSPÖ buffer material as a function of the water content	15
Fig. 4.4	Emplacement of moisturized backfill into measurement cell for determination of material resistivity	18
Fig. 4.5	Measurement set-up for determination of backfill resistivity	19
Fig. 4.6	Resistivity of compacted backfill samples versus water content	20
Fig. 4.7	Correlation between resistivity and saturation on granite samples from HRL Äspö	21
Fig. 4.8	Experimental set-up of percolation experiment	23
Fig. 4.9	Composition of Äspö solution. All concentrations in mg/l	25
Fig. 4.10	Change of normality of percolate. Note that normality is constantly a bit higher than that of inflowing solution	26
Fig. 4.11	Na-concentration in Äspö-solution after penetrating compacted MX-80	26
Fig. 4.12	K-concentration in Äspö-solution after penetrating compacted MX-80	27
Fig. 4.13	Mg-concentration in Äspö-solution after penetrating compacted MX-80	27
Fig. 4.14	Ca-concentration in Äspö-solution after penetrating compacted MX-80	28

Fig. 4.15	Cl-concentration in Äspö-solution after penetrating compacted MX-80.....	28
Fig. 4.16	SO ₄ -concentration in Äspö-solution after penetrating compacted MX-80.....	29
Fig. 4.17	Mineral saturation states in percolates	32
Fig. 4.18	Geoelectric modelling of the prototype repository backfill: Rectangular model without surrounding rock (left: input model, right: inversion result)	34
Fig. 4.19	Geoelectric modelling of the prototype repository backfill: Rectangular model with surrounding rock (left: input model, right: inversion result)	35
Fig. 4.20	Geoelectric modelling of the prototype repository backfill: Elliptic drift model with surrounding rock (left: input model, right: inversion result); "double cross" electrode arrangement (x = electrode locations)	35
Fig. 4.21	Geoelectric modelling of the prototype repository buffer with the original electrode arrangement (left: input model, right: inversion result).....	36
Fig. 4.22	Geoelectric modelling of the prototype repository buffer with additional central chain (left: input model, right: inversion result)	36
Fig. 4.23	Geoelectric modelling of the prototype repository buffer with additional horizontal chain (left: input model, right: inversion result)	37
Fig. 4.24	Geoelectric modelling of the prototype repository buffer with the new electrode arrangement: dry buffer (left: input model, right: inversion result)	37
Fig. 4.25	Geoelectric modelling of the prototype repository buffer with the new electrode arrangement: partially wetted buffer (left: input model, right: inversion result)	38
Fig. 4.26	Geoelectric modelling of the prototype repository buffer with the new electrode arrangement: enlarged wet buffer zone (left: input model, right: inversion result)	38
Fig. 5.1	Geoelectric Measurement System RESECS	40

Fig. 5.2	Overview of electrode arrangements in the Prototype Repository	42
Fig. 5.3	Design of a drift electrode.....	43
Fig. 5.4	Design of an ELOCAB cable (diameter of multi-wire cable: 27.5 mm, diameter of single wire: 2.7 mm).....	43
Fig. 5.5	GISMA plug.....	44
Fig. 5.6	Principle design of an electrode chain in the drift.....	44
Fig. 5.7	ELOCAB cable at head flange of a lead-through borehole	45
Fig. 5.8	Installation of electrode array in the backfill in Section I. Left: installation of cables in trenches, centre: trenches partially covered with fine-grained bentonite, right: completely embedded electrode array.....	45
Fig. 5.9	Double cross electrode arrangement in the backfill	46
Fig. 5.10	Electrode chains at top of deposition hole #5	47
Fig. 5.11	Installation of electrode chain in the buffer at top of borehole 5	47
Fig. 5.12	Arrangement of electrodes in the buffer at the top of deposition hole #5 and in the adjacent rock (o = electrodes).....	48
Fig. 5.13	Design of electrode chain in the buffer	48
Fig. 5.14	Design of electrode chains in the rock (note the additional 12 electrodes for buffer monitoring at the upper part of the left-hand borehole)	50
Fig. 5.15	Insertion of an electrode chain into a measuring borehole in the rock between deposition hole #5 and #6 in Section II.....	50
Fig. 6.1	Geoelectric tomograms of the backfill in Section I – 2001 – 2007.....	52
Fig. 6.2	Geoelectric tomograms of the backfill in Section I – 2007 – 2013.....	54

Fig. 6.3	Resistivity tomograms of the backfill in Section I, August 2010. Left: taking into account all active electrodes, right: neglecting the electrodes close to the roof.....	55
Fig. 6.4	Geoelectric tomograms of the backfill in Section II – 2003 – 2010.....	56
Fig. 6.5	Geoelectric tomograms of the buffer at the top of deposition hole #5	58
Fig. 6.6	Resistivity distribution along the electrode chains in the rock – August 2002.....	59
Fig. 6.7	Resistivity distribution along the electrode chains in the rock – 2003/2004..	60
Fig. 6.8	Resistivity distribution along the electrode chains in the rock – 2004-2006..	61
Fig. 6.9	Resistivity distribution along the electrode chains in the rock – 2007-2009..	62
Fig. 6.10	Resistivity distribution along the electrode chains in the rock – 2010.....	63
Fig. 7.1	Plexiglass tube with backfill material and electrodes (left) and resistivity tomograms obtained after flooding to 70 % height (centre and right, for two longitudinal sections)	66
Fig. 8.1	Electrodes from the backfill in Section II showing surface corrosion	68
Fig. 8.2	Core section from the top central buffer of deposition hole #5 with embedded electrode chain	68
Fig. 8.3	Electrode chain embedded in the buffer	69
Fig. 8.4	Retrieved electrode chain.....	69
Fig. 8.5	Location of samples for water content analysis with colour coded results....	70
Fig. 8.6	Clay Technology results for water content and saturation of the upper buffer of deposition hole #5, with supplement of GRS water content values for the buffer cores (modified after /JOH 11/)	72

List of tables

Tab. 4.1	Composition of the ÄSPÖ solution [mmol/l] used for sample preparation	12
Tab. 4.2	Water content and size of the prepared MX-80 samples and of the original buffer samples	12
Tab. 4.3	Summary of the water content and the resistivities of the compacted MX-80 samples and the original ÄSPÖ buffer material	16
Tab. 4.4	Water content and achieved dry density of backfill samples	18
Tab. 4.5	Planning data for percolation experiment	24
Tab. 8.1	Measured water content of buffer core samples	71

**Gesellschaft für Anlagen-
und Reaktorsicherheit
(GRS) gGmbH**

Schwertnergasse 1
50667 Köln

Telefon +49 221 2068-0

Telefax +49 221 2068-888

Forschungszentrum

85748 Garching b. München

Telefon +49 89 32004-0

Telefax +49 89 32004-300

Kurfürstendamm 200

10719 Berlin

Telefon +49 30 88589-0

Telefax +49 30 88589-111

Theodor-Heuss-Straße 4

38122 Braunschweig

Telefon +49 531 8012-0

Telefax +49 531 8012-200

www.grs.de